Master's Thesis

# Systematic study of $e^+e^- \to t\bar{t}$ at the ILC using full simulation of the ILD Detector and determination of anomalous electroweak coupling of top quarks

Yuichi Okugawa

Department of Physics
Graduate School of Science
Tohoku University
2019

*“It doesn’t matter how beautiful your theory is, it doesn’t matter how smart you are. If it doesn’t agree with experiment, it’s wrong.”*

Richard P. Feynman

TOHOKU UNIVERSITY

# *Abstract*

Graduate School of Science and Faculty of Science
Department of Physics

Master of Science

by Yuichi Okugawa

The heavy quarks have masses comparable to the electroweak vacuum expectation value.With a mass of 173 GeV the top quark is the heaviest known elementary particle today. Anomalies in observables for b-quarks have been reported by LEP and may get amplified for the 40 times heavier top quark. Therefore, the precise measurements on the heavy quark properties is essential for the indirect searches of the new particle beyond the Standard Model predictions to differentiate them from the various other theories.

In this thesis, the $e^+e^- \to t\bar{t}$ process with polarized beams at $\sqrt{s} = 500$ GeV is studied using the full simulation of the ILD detector. Results for both semi-leptonic channel ($t\bar{t} \to b\bar{b}W^+W^- \to b\bar{b}q\bar{q}\ell\nu$) and full-hadronic channel ($t\bar{t} \to b\bar{b}W^+W^- \to b\bar{b}q\bar{q}q\bar{q}$) are presented. The proper measurement of the angular distribution of the final state require a clean distinction between $t$ and $\bar{t}$ For the semi-leptonic channel, isolated lepton charge, the vertex charge and kaon charge are used in different combinations to identify the reconstructed top charge. At the total integrated luminosity of $\mathcal{L} = 3200$ fb$^{-1}$, with electron and positron polarization state of $(\mathcal{P}_{e^-}, \mathcal{P}_{e^+}) = (\pm 0.8, \pm 0.3)$, the polar angle distributions of the top-quark are reconstructed in order to calculate the forward-backward asymmetry parameter $A^t_{FB}$. As a result, $A^t_{FB} = 0.345$ is obtained for $(\mathcal{P}_{e^-}, \mathcal{P}_{e^+}) = (-0.8, +0.3)$ polarization with statistical uncertainty of $\delta_{A^t_{FB}} = 2.48 \times 10^{-3}$. For the $(\mathcal{P}_{e^-}, \mathcal{P}_{e^+}) = (+0.8, -0.3)$ polarization, $A^t_{FB} = 0.369$ with statistical uncertainty of $\delta_{A^t_{FB}} = 1.96 \times 10^{-3}$ was obtained. For the first time, the reconstructed $b$ quark polar angle distribution decayed from top quarks was presented. This revealed the acceptance drop at the high polar angle due to the poor $b$-jet reconstruction. Nonetheless, the reconstruction was accurately done for $|\cos\theta < 0.8|$

region, indicating vertex charge measurements as efficient as those for the isolated lepton charge measurements. For the full-hadronic channel, $t\bar{t}$ were distinguished by the kaon and vertex charge only. As a result, $A^t_{FB} = 0.322$ was obtain for $(\mathcal{P}_{e^-}, \mathcal{P}_{e^+}) = (-0.8, +0.3)$ polarization with statistical uncertainty of $\delta_{A^t_{FB}} = 2.76 \times 10^{-3}$.

# *Acknowledgements*

Upon completing this study, I had many supports from people in the Tohoku University, KEK and LAL as a part of ILC working group.

Firstly, I would like to thank Professor Hitoshi Yamamoto for supervising my thesis, as well as arranging internships and trips to international conferences. This helped me gain some experience in presentation and gave me confidence for growing up as a researcher. I also like to pay my special regards to Professor Roman Pöschl for directly supervising this study spending major time to review this thesis. He also took care of my stay at France during the internship at LAL, which led me to decide to pursue my PhD there. I would also like to show my deepest gratitude to Professor Richard Francois, who gave many advise for this thesis. I wish to show my gratitude to Dr. Yonamine for help resolving the technical difficulties. I would also like to thank Professor Sanuki and Dr. Nagamine for teaching me the basics of the detectors. I am indebted to Dr. Adrian Irles, who helped me a lot with every details to this analysis. I am also grateful that Yo Sato, senior PhD student, help me understand the pre-studies to this research, as well as underlying physics. I would like to thank Victor Lohezic, an intern student from the University of Paris-Saclay, who helped me with the analysis for this study using right handed polarized beam. I wish to express my gratitude to Kaori Kobayashi for arranging business trip to conferences and internships. I would also like to show my greatest gratitude to my family who have been supportive during my Master's course and supported my decision for going to the PhD.

I wish to thank all the people whose assistance was a milestone in the completion of this project.

# Contents

# List of Figures

# List of Tables

# Abbreviations

| | |
|---|---|
| **ECAL** | **E**lectromagnetic **CAL**orimeter |
| **ETD** | **E**ndplate of the **T**PC **D**etector |
| **FTD** | **F**orward **T**racking **D**etector |
| **HCAL** | **H**adronic **CAL**orimeter |
| **IDR** | **I**LD **D**esign **R**eport |
| **ILC** | **I**nternational **L**inear **C**ollider |
| **ILD** | **I**nternational **L**arge **D**etector |
| **MC** | **M**onte **C**arlo |
| **NLO** | **N**ext to **L**eading **O**rder |
| **PV** | **P**rimary **V**ertex |
| **QCD** | **Q**uantum **C**hromo **D**ynamics |
| **QED** | **Q**uantum **E**lectro **D**ynamics |
| **SV** | **S**econdary **V**ertex |
| **SET** | **S**ilicon **E**xternal **T**racker |
| **SIT** | **S**ilicon **I**nner **T**racker |
| **TMVA** | **T**oolkit for **M**ulti**V**ariate Data **A**nalysis |
| **TPC** | **T**ime **P**rojection **C**hamber |
| **VXD** | **V**erte**X** **D**etector |

# Chapter 1

# Introduction

## 1.1 Motivation

The mass hierarchy of fermions cannot be explained within the Standard Model of particle physics. In particular the top quark is the heaviest elementary particle known today. With a mass comparable to the scale of electroweak breaking. Within the Standard Model the top forms an iso-doublet with an anomaly in the measurement of the forward-backward asymmetry $A^t_{FB}$ is still unresolved today. Many models for physics beyond the Standard Model explain the mass hierarchy by the existence of extra dimensions implying in particular modifications of the left and right handed electroweak couplings of the heavy quarks. A linear collider with polarized beams is the adequate tool to study the electroweak couplings of heavy quarks and to detect the onset of new physics.

## 1.2 The Standard Model

The Standard Model (SM) of particle physics is a theoretical framework to understand elementary particles, along with interactions among them via three fundamental forces: electromagnetic, weak and strong force. Conservation laws as e.g. charge conservation in electromagnetism imply the invariance of the theory w.r.t. symmetry operations that are represented by unitary symmetry groups. Without going into the details here. the relevant symmetry groups are U(1) for QED, SU(2) for the weak force and SU(3) for the strong force. Intuitively this can understood by the fact that for fundamental fermions (see Sec. 1.2.1) there exist one electrical charge state, two isospin states and three color states. In particular, SM combines the theory of Quantum Chromo Dynamics (QCD) for strong interactions, with Wienberg-Salam which constructs framework of $SU(2) \times U(1)$, leading the formation of $SU(3) \times SU(2) \times U(1)$ gauge symmetry. Figure 1.1 shows the list of particle contents of the Standard Model.

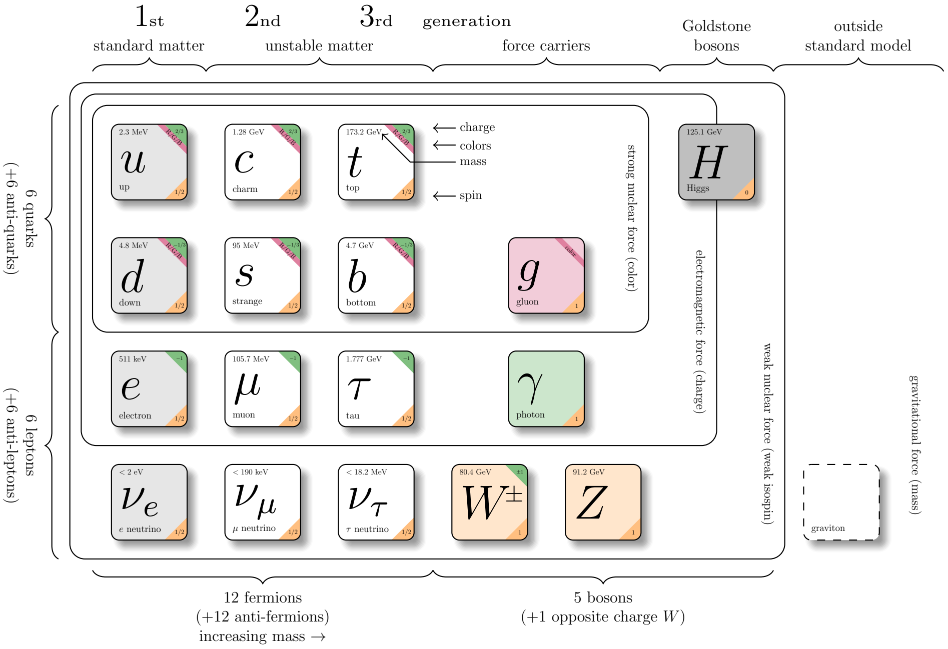

Figure 1.1: The Standard Model table

### 1.2.1 Fermions

Fermions are the constituents of matters with spin-1/2, and they are categorized in two subgroups, quarks and leptons. Each group has 6 members subdivided into three generations. In the Standard Model, they are organized in left-handed doublets and right-handed singlets which is under $SU(2)_L$ with charges under $U(1)_Y$ where $Y$ represents hypercharge. Electric charge, $Q$, is now know to be coming from the breaking of the electroweak group of $SU(2)_L \times U(1)_Y \to U(1)_{EM}$, where $U(1)_{EM}$ is what we know as electromagnetic group. The generator of $SU(2)_L$ is the weak isospin ($I_3^L$). Together with hypercharge, they form electric charge in following manner:

$$Q = I_3^L + \frac{1}{2}Y \tag{1.1}$$

List of combination between isospin and hypercharge is shown in the table 1.1. Note that right-handed neutrinos do not possess any quantum numbers thus they do not interact with the Standard Model particles.

| | I | II | III | $I_3^L$ | Y | Q |
|---|---|---|---|---|---|---|
| Leptons | $e_L$ | $\mu_L$ | $\tau_L$ | -1/2 | -1 | -1 |
| | $\nu_{eL}$ | $\nu_{\mu L}$ | $\nu_{\tau L}$ | +1/2 | -1 | 0 |
| | $e_R$ | $\mu_R$ | $\tau_R$ | 0 | -2 | -1 |
| | $\nu_{eR}$ | $\nu_{\mu R}$ | $\nu_{\tau R}$ | 0 | 0 | 0 |
| Quarks | $u_L$ | $c_L$ | $t_L$ | +1/2 | +1/3 | +2/3 |
| | $d_L$ | $s_L$ | $b_L$ | -1/2 | +1/3 | -1/3 |
| | $u_R$ | $c_R$ | $t_R$ | 0 | +4/3 | +2/3 |
| | $d_R$ | $s_R$ | $b_R$ | 0 | -2/3 | -1/3 |

Table 1.1: Hyper charge and isospins of fermions. I, II, III shows the generations of the fermions.

### 1.2.2 Boson

All bosons have integer number of spin. In the Standard Model, vector bosons, which have spin 1, are the carriers of forces. The massless photon transmits the electromagnetic force, the massive vector bosons, $Z^0$ and $W^{\pm}$, transmit the electroweak force, and gluon transmits the strong force.

## 1.3 Standard Model Interactions

### 1.3.1 Electromagnetic Interaction

The classical mechanical definition of the electromagnetism is described by the Maxwell equations. The extension of this equation, Quantum Electrodynamics

(QED) explores the quantum field theory by defining the gauge group $U(1)_{EM}$. The equation of the motion is described using Lagrangian density, $\mathcal{L}$, and two fermions fields $\psi(x)$ are defined as below:

$$\mathcal{L} = i\bar{\psi}(x)\gamma^{\mu}\partial_{\mu}\psi(x) - m\bar{\psi}(x)\psi(x) \tag{1.2}$$

where the $\gamma^{\mu}$ is the gamma matrices and $m$ is the mass of the fermion. The theory should be invariant under local U(1) gauge transformation $e^{i\theta}\psi$

$$\psi(x) \rightarrow e^{i\theta(x)}\psi(x) \tag{1.3}$$

This would cause no difference in the mass term. Kinetic term, on the other hand, changes the Lagrangian density and becomes:

$$i\bar{\psi}(x)\gamma^{\mu}\partial_{\mu}\psi(x) \rightarrow i\bar{\psi}(x)\gamma^{\mu}\partial_{\mu}\psi(x) - \bar{\psi}(x)\gamma^{\mu}\psi(x)\partial_{\mu}\theta(x) \tag{1.4}$$

where we are left with extra second term. In order to preserve the local gauge symmetry, vector field $A_{\mu}$, which is also known as photon field, is introduced as following:

$$-eA_{\mu}\bar{\psi}\gamma^{\mu}\psi \tag{1.5}$$

where the local gauge transformation is done by

$$A_{\mu}(x) \rightarrow A_{\mu}(x) - \frac{1}{e}\partial^{\mu}\theta(x) \tag{1.6}$$

The eq. 1.5 will then transformed as:

$$-eA_{\mu}\bar{\psi}\gamma^{\mu}\psi \rightarrow -eA_{\mu}\bar{\psi}\gamma^{\mu}\psi + \bar{\psi}(x)\gamma^{\mu}\psi(x)\partial_{\mu}\theta(x) \tag{1.7}$$

which cancels the second term in the eq. 1.4. After introducing covariant derivative operator as

$$\partial_{\mu} \rightarrow D_{\mu} = \partial_{\mu} - ieA_{\mu} \tag{1.8}$$

the the final local gauge invariant Lagrangian density can be written as:

$$\mathcal{L} = \bar{\psi}(x)(i\gamma^{\mu}D_{\mu} - m)\psi(x) - \frac{1}{4}F_{\mu\nu}F^{\mu\nu} \tag{1.9}$$

where

$$F_{\mu\nu} = \partial_\mu A_\nu - \partial_\nu A_\mu \tag{1.10}$$

is the strength tensor for the photon field. When such field is quantized, this is called *gauge boson*.

### 1.3.2 Electroweak Interactions

The first observation of the weak interaction was recorded from the $\beta$ decay ($n \to p\ e^- \nu_e$), when the missing energies taken by the neutrino raised the suspicion that there's such an interaction. The full experiment was conducted by Chien-Shiung Wu, which led to the discovery that such interaction violates the conservation of parity [3]. The robust framework of the electroweak theory was formed after the unification of electromagnetic and weak interactions by Glashow in 1961 [4]. The actual model was proposed by Weinberg and Salam [5, 6]. This theory motivated the introduction of charged vector bosons, $W^\pm$, and neutral vector bosons, $Z^0$.

Weak interaction is particularly related to the particle chirality, which can be seen from the weak current as below.

$$\bar{\psi}\gamma^\mu(1-\gamma_5)\psi \tag{1.11}$$

This is also known as a vector - axial structure (V-A structure). Using vector field $W_\mu^i$ $(i = 1, 2, 3)$ of $SU(2)_L$ with coupling g and vector field $B_\mu$ of $U(1)_Y$ with coupling g', the Lagrangian density of the electroweak interaction is described in the equation below.

$$\mathcal{L}_{EW} = -ig(J^i)^\mu W_\mu^i - i\frac{g'}{2}(j^Y)^\mu B_\mu \tag{1.12}$$

with weak isospin current ($J_\mu^i$) and hypercharge current ($j_\mu^Y$)

$$J_\mu^i = \bar{\psi}\frac{\tau^i}{2}\gamma_\mu\frac{1-\gamma^5}{2}\psi \tag{1.13}$$

$$j_\mu^Y = \bar{\psi}Y\gamma_\mu\psi \tag{1.14}$$

where $\tau^i$ ($i = 1, 2, 3$) are Pauli matrices and $Y$ is hypercharge. After introducing mass eigenstate of $W^\pm_\mu$ as

$$W^\pm_\mu = \frac{1}{\sqrt{2}}(W^1_\mu \pm iW^2_\mu) \tag{1.15}$$

mixing of electromagnetic and weak interaction can be expressed in following form:

$$\begin{pmatrix} A^\mu \\ Z^\mu \end{pmatrix} = \begin{pmatrix} \cos\theta_w & \sin\theta_w \\ -\sin\theta_w & \cos\theta_w \end{pmatrix} \begin{pmatrix} B^\mu \\ W^\mu_3 \end{pmatrix} \tag{1.16}$$

where $\theta_w$ is the Weinberg angle. Note that the mixing between $SU(2)_L \times U(1)_Y$ enables the interaction of $Z$ and $A$ with left and right handed particles, while $W^\pm$ can only couple with left handed particles.

### 1.3.3 The Higgs Mechanism

In the naive description of the theory of the Standard Model, spin-1 gauge bosons were assumed to be massless. However in the real experiments, $W^\pm$ and $Z^0$ boson masses are measured to be 80.4 GeV and 91.2 GeV, respectively [7]. The acquisition of the mass can be explained by the spontaneous symmetry breaking yeilding the Higgs mechanism.

Consider a complex scalar field $\phi$ as

$$\phi = \frac{1}{\sqrt{2}}(\phi_1 + i\phi_2) \tag{1.17}$$

and the Lagrangian of this can be written as

$$\mathcal{L} = (\partial_\mu\phi)^*(\partial^\mu\phi) - V(\phi) \tag{1.18}$$

where the potential $V(\phi)$ is

$$\begin{aligned} V(\phi) &= \mu^2(\phi^*\phi) + \lambda(\phi^*\phi)^2 \\ &= \frac{1}{2}\mu^2(\phi_1^2 + \phi_2^2) + \frac{1}{4}\lambda(\phi_1^2 + \phi_2^2)^2 \end{aligned} \tag{1.19}$$

and combined with eq. 1.18, the full expression of the Lagrangian in terms of two real scalar fields ($\phi_1$ and $\phi_2$) becomes:

$$\mathcal{L} = \frac{1}{2}(\partial_\mu \phi_1)(\partial^\mu \phi_1) + \frac{1}{2}(\partial_\mu \phi_2)(\partial^\mu \phi_2) - \frac{1}{2}\mu^2(\phi_1^2 + \phi_2^2) - \frac{1}{4}\lambda(\phi_1^2 + \phi_2^2)^2 \qquad (1.20)$$

In order to have a finite minimum solution, $\lambda > 0$. This potential will have different minimum values depending on whether $\mu > 0$ or $\mu < 0$. In the case of $\mu > 0$, the minimum value of the potential is $V(\phi) = 0$, while $\mu < 0$ makes $V(\phi) = 0$ to be unstable equilibrium. In fact the minimum value of the potential when $\mu < 0$ is $V(\phi) = \sqrt{-\mu^2/\lambda}$ which we defined to be $\nu$. On the right hand side of the figure 1.2, one can see the bottom of the potential ($\phi_1^2 + \phi_2^2 = \nu^2$) and this corresponds to the physical vacuum state. This does not have the symmetry properties that came with the original Lagrangian, known as spontaneous symmetry breaking.

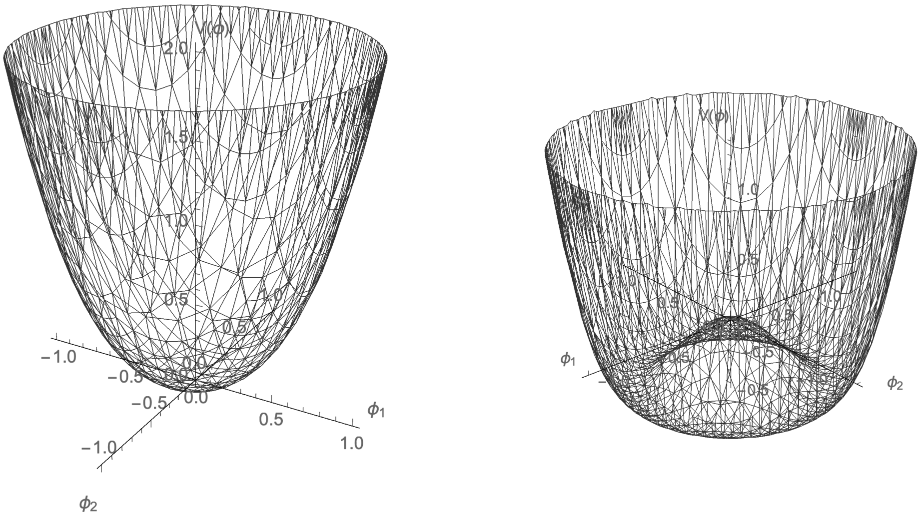

FIGURE 1.2: The $V(\phi) = \mu^2(\phi^*\phi) + \lambda(\phi^*\phi)^2$ potential with $\mu > 0$ (*left*) and $\mu < 0$ (*right*).

Now, one needs to apply the $SU(2)_L \times U(1)_Y$ gauge symmetry to generate the masses of the electroweak gauge bosons. This is called *the Higgs mechanism.* First, the complex $SU(2)_L$ isospin doublet is introduced as following:

$$\phi = \begin{pmatrix} \phi^+ \\ \phi^0 \end{pmatrix}, \quad \langle 0|\phi|0\rangle = \frac{1}{\sqrt{2}}\begin{pmatrix} 0 \\ \nu \end{pmatrix} \qquad (1.21)$$

where $\phi^+$ ($(\phi^+)^* = \phi^-$) and $\phi^0$ are the charged and neutral scalar fields, respectively. The Lagrangian to the doublet of the complex scalar field can be written similar to the eq. 1.18 as

$$\mathcal{L} = (\partial_\mu \phi)^\dagger (\partial^\mu \phi) - V(\phi) \tag{1.22}$$

with potential

$$V(\phi) = \mu^2(\phi^\dagger \phi) + \lambda(\phi^\dagger \phi)^2 \tag{1.23}$$

In order to keep the local gauge symmetry, covariant derivative $D_\mu$ is introduced

$$\partial_\mu \to D_\mu = \partial_\mu + igT_i W_\mu^i + ig'\frac{Y}{2}B_\mu \tag{1.24}$$

where $T_i$ are the Pauli matrices and hence generators of the $SU(2)$ symmetry. After the spontaneous symmetry breaking, there will be massive gauge bosons, enabling $W^\pm$ and $Z^0$ to have longitudinal degree of freedom as following

$$\phi = \frac{1}{\sqrt{2}} \begin{pmatrix} 0 \\ \nu + h \end{pmatrix} \tag{1.25}$$

where $h$ is the quantum fluctuations around the vacuum expectation value, known as the Higgs field. Substituting eq. 1.24 into eq. 1.22 and focusing on the $(D_\mu \phi)^\dagger (D^\mu \phi)$ part gives

$$(D_\mu \phi)^\dagger (D^\mu \phi) = \frac{1}{2}(\partial_\mu h)^2 + \frac{1}{8}g^2(\nu + h)^2 |W_\mu^1 + iW_\mu^2|^2 + \frac{1}{8}(\nu + h)^2 |gW_\mu^3 - g'B_\mu|^2 \tag{1.26}$$

Mass terms for gauge bosons appear as quadratic terms

$$\frac{1}{8}\nu^2 g^2 (W_\mu^1 W^{1\mu} + W_\mu^2 W^{2\mu}) = \frac{1}{2}M_W^2 (W_\mu^1 W^{1\mu} + W_\mu^2 W^{2\mu}) \tag{1.27}$$

and the masses of $W^1$ and $W^2$ spin-1 fields are determined to be

$$M_W = \frac{1}{2}\nu g \tag{1.28}$$

Using the relation in eq. 1.16,

$$Z_\mu = \frac{gW_\mu^3 - g'B_\mu}{\sqrt{g^2 + g'^2}}, \quad A_\mu = \frac{gW_\mu^3 + g'B_\mu}{\sqrt{g^2 + g'^2}} \tag{1.29}$$

and the masses of neutral gauge bosons can be identified as

$$M_Z = \frac{1}{2}\nu\sqrt{g^2 + g'^2}, \quad M_A = 0 \tag{1.30}$$

Thus $W^{\pm}$ and $Z^0$ obtains mass through the Higgs mechanism while photon remains massless.

# Chapter 2

# International Linear Collider

## 2.1 Introduction to ILC

In the course of particle physics history, particle accelerators played the huge role in the discovery of new physics and particles. There are two types of colliders: lepton and hadron colliders. The Large Hadron Collider (LHC) is the biggest and the most powerful proton-proton collider of the world. The discovery of a scalar particle with features as expected for the Standard Model Higgs Boson can be considered as the completion of the Standard Model. The large range of centre-of-mass energies swept over by the LHC allow for scanning the LHC data for signals of new physics, such as new resonances or intriguing signals with missing mass. The new scalar particles has to be examined with higher precision than available at LHC. The absence of clear signals for new physics calls for a closer look at the quantum fluctuations. Both call arguments for high precision measurements as they are available by lepton colliders and in particular by $e^+e^-$ colliders.

Lepton collider has multiple advantages over hadron colliders, such as well-known initial state of colliding particles and comparatively small and well calculable QCD backgrounds. Circular colliders are heavily limited by energy loss due to synchrotron radiation. The energy loss per turn is

$$E_{rad} \propto \frac{E^4}{m^4 r} \tag{2.1}$$

where $E$ is energy, $m$ is the particle mass and $r$ is the curvature. As shown in eq. 2.1, radiated energy due to synchrotron radiation, $E_{rad}$ is particularly significant

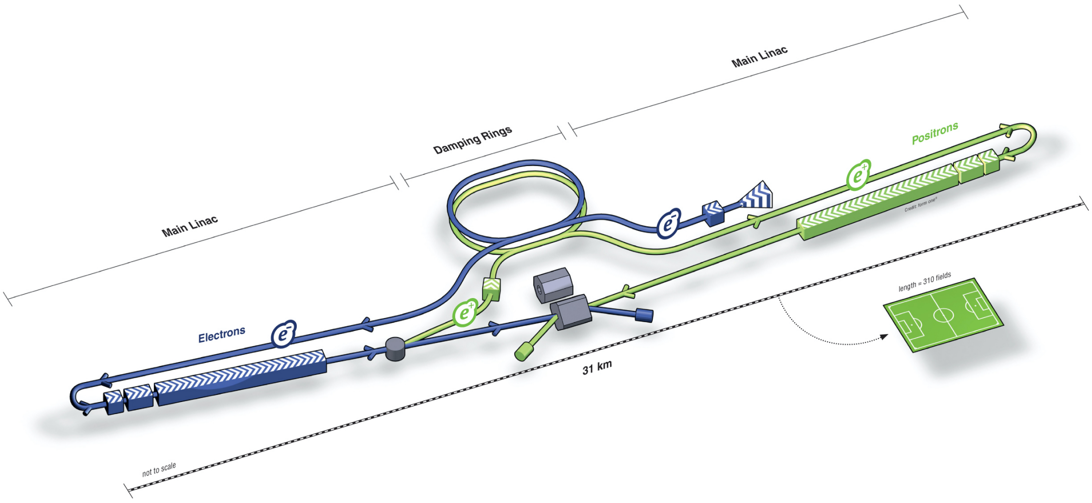

FIGURE 2.1: Layout of the ILC

when dealing with lighter particles as electrons. The International Linear Collider (ILC) [8] is electron-positron collider which is expected to run at the center of mass energy of 250 GeV at the beginning. It does not suffer from the synchrotron radiation and initial states of electron and positron beams can be controlled. After the run at the 250 GeV, the accelerator will be extended to achieve the energy of 500 GeV and beyond.

## 2.2 Physics Case of the ILC

One of the substantial goals to be achieved by ILC is the precision measurements of particle properties. ILC facilitates the model independent search of the electroweak parameters. Table 2.1 summarizes key physics processes at different centre-of-mass energies available with the ILC

At the energy of 250 GeV, where the cross section of the Higgs-strahlung process is the largest, it is expected to measure the Higgs boson mass with high precision by calculating the recoil mass. Higgs couplings to Standard Model fermions and the Z can be determined at the 1% level. The recoil technique opens also sensitivity to invisible Higgs decays. Studies of the Higgs boson are extended to the higher energies for the Higgs self-coupling and the coupling with the top quark, also known as top Yukawa coupling.

| Energy | Reaction | Objective |
|---|---|---|
| 91 GeV | $e^+e^- \to Z^0$ | $Z^0$ physics |
| 160 GeV | $e^+e^- \to WW$ | $W^\pm$ mass precision |
| 250 GeV | $e^+e^- \to Z^0H$ | Precision Higgs coupling |
| 350 GeV | $e^+e^- \to t\bar{t}$ | Top mass precision |
|  | $e^+e^- \to \nu\bar{\nu}$ | Precision Higgs coupling |
| 500 GeV | $e^+e^- \to t\bar{t}$ | Top coupling |
|  | $e^+e^- \to t\bar{t}H$ | Top Higgs coupling |
|  | $e^+e^- \to Z^0HH$ | Higgs self coupling |
| 1 TeV | $e^+e^- \to \nu\bar{\nu}t\bar{t}$ | Composite Higgs and Top |

Table 2.1: Main physical process that is expected to be seen at the ILC

Investigation of top quarks also plays a crucial role for the ILC project. A scan at the $t\bar{t}$ threshold around 350 GeV allows for extracting a theoretically well defined value of the top quark mass to a precision of at least 50 MeV. The coupling between gauge boson and top quark is particularly sensitive to the new physics and these processes motivate the studies presented in this thesis.

## 2.3 The Accelerator Apparatus

### 2.3.1 Electron Source

Polarized electron beam, which can satisfy the requirements for the bunch train, must be produced at electron source. At the ILC, the beam is produced by laser illuminating the GaAs photocathode inside the DC gun. When polarized photons are incident upon the photocathode, polarized photoelectrons will be emitted due to photoelectric effect and it is expected to have maximum of 80% polarization. These photoelectrons will form polarized electron bunch, which will be delivered to the normal conducting structure, accelerating up to 76 MeV. It will then go through superconducting linac while aligning the electrons' spin directions perpendicular to the beam direction and accelerating them to 5 GeV. Finally, the bunch will be injected to the Damping Ring.

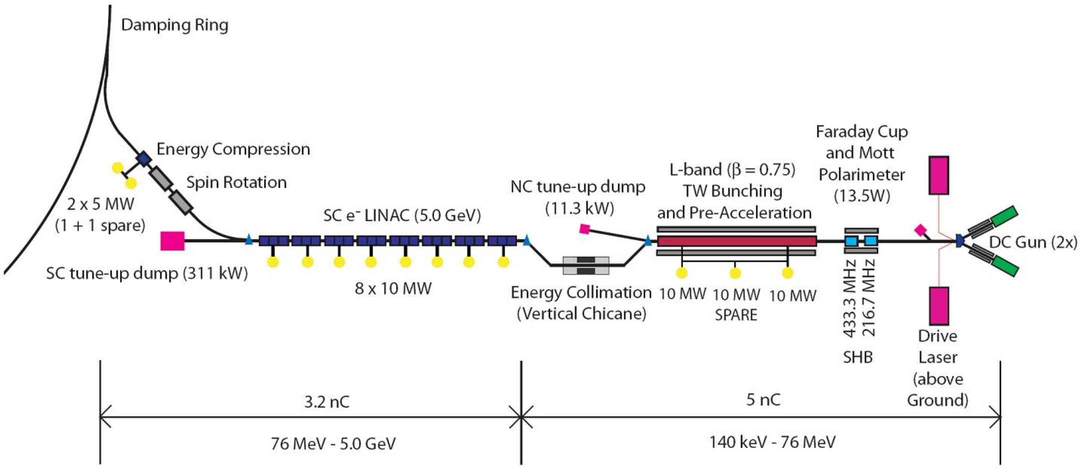

Figure 2.2: Sketch of electron source instruments.

### 2.3.2 Positron Source

Electron beam that passed the main linac will go through superconducting helical undulator which deflects the beam direction, emitting bremsstrahlung radiation as a result. These photons with energy ranging between 10 - 30 MeV will hit the rim of the rotating titanium alloy target, pair producing $e^+e^-$ as a result. After hitting the target, positrons are separated from electrons and photons by applying magnetic field at the end of the RF cavities. Similar to the electrons, positrons will also go through normal conducting and superconducting linac to be accelerated from 125 MeV to 5 GeV. Note that with this method, positrons will inherit the polarization of the photon, obtaining at least 30% polarization through the process.

### 2.3.3 Damping Ring

Electron and positron beam passes through damping ring with 3.2 km circumference size, each operating at the beam energy of 5 GeV. Due to its physical structure, ILC relies on each single bunch crossing, unlike LHC which circulates bunches until they collide. Thus it is essential to increase collision probability in

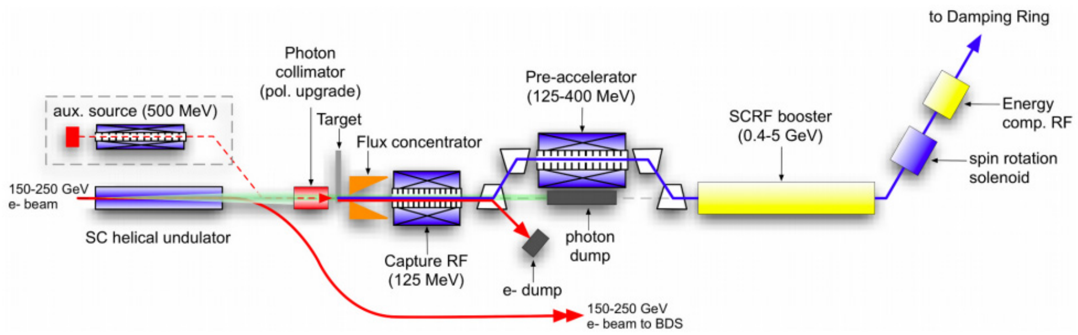

**Figure 3.4.** Overall Layout of the Positron Source, located at the end of the electron Main Linac.

FIGURE 2.3: Positron source setting.

each bunch crossing by minimizing the beam emittance. Damping ring contributes to this by minimizing the phase space of the beam. When the beam circulates inside the damping ring, the one with higher momentum loses its energy due to the emission of synchrotron radiation, while the lower one obtains the energy by the acceleration provided by the ring. Damping ring layout is shown in the Fig. 2.4.

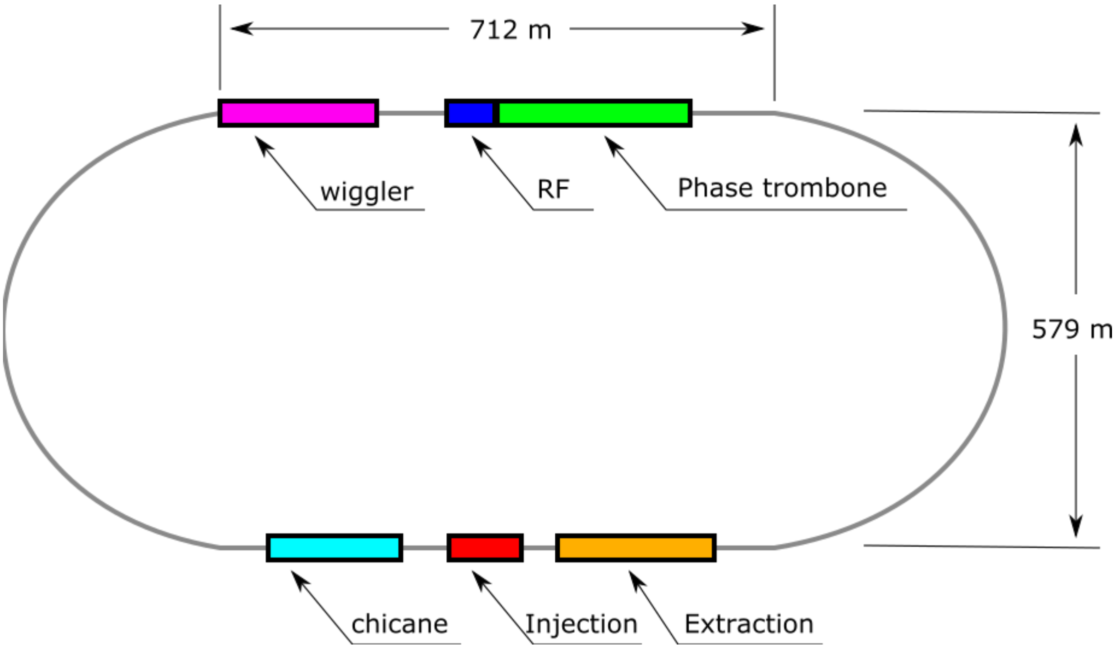

FIGURE 2.4: Layout of the damping ring.

### 2.3.4 Main Linac

There are two main linacs located at the both sides of the ILC, each accelerates electron and positron beams. Both of which are 11 km long, containing 7,400 of 1.3 GHz superconducting nine-cell niobium cavities, operating at 2 K (Fig. 2.5).

These cavities accelerate beams from 15 GeV to 250 GeV at maximum, with average acceleration gradient of 31.5 MeV/m.

FIGURE 2.5: Cryomodule that is planned to implement niobium cavities.

### 2.3.5 Beam Delivery System

Beam delivery system governs the work of delivering the beam from the electron and positron source, while converging the beam at the collision point. After the collision, it will deliver the spent beam to the beam dump.

# Chapter 3

# International Large Detector

## 3.1 Introduction to ILD

International large detector (ILD) is a concept for a detector proposed for the ILC. The current baseline foresees that both detectors are operated alternately using a push-pull scheme for moving the detectors. ILD is steadily optimized, where currently the two designs are being evaluated: small and large detector models. This study contributed to the benchmarking studies by evaluating the performance of two models for the $t\bar{t}$ analysis. In this thesis, the analysis with large detector model is shown. ILD consists of 6 sub-detectors in the central region and 3 forward calorimetry systems. The cross sectional view of the ILD is shown in the fig. 3.1.

## 3.2 Particle Flow Algorithm

In many cases the $e^+e^-$ collisions lead to final states with collimated sprays of hadrons called jets. The jets are often the decay products of unstable SM particles as W, Z, H and top. The correct association of the jets to their respective mother particles requires unprecedented jet energy resolution. Particle Flow Algorithms (PFA) are designed to reconstruct particles by retrieving the information from tracker and calorimeter. The example of this reconstruction scheme is shown in the fig. 3.2. The design goal of the ILD is to achieve the jet energy resolution in order of 3-4% over the entire jet energy range. This is supposed to be achieved with PFA which has the goal to measure each individual particle's final states.

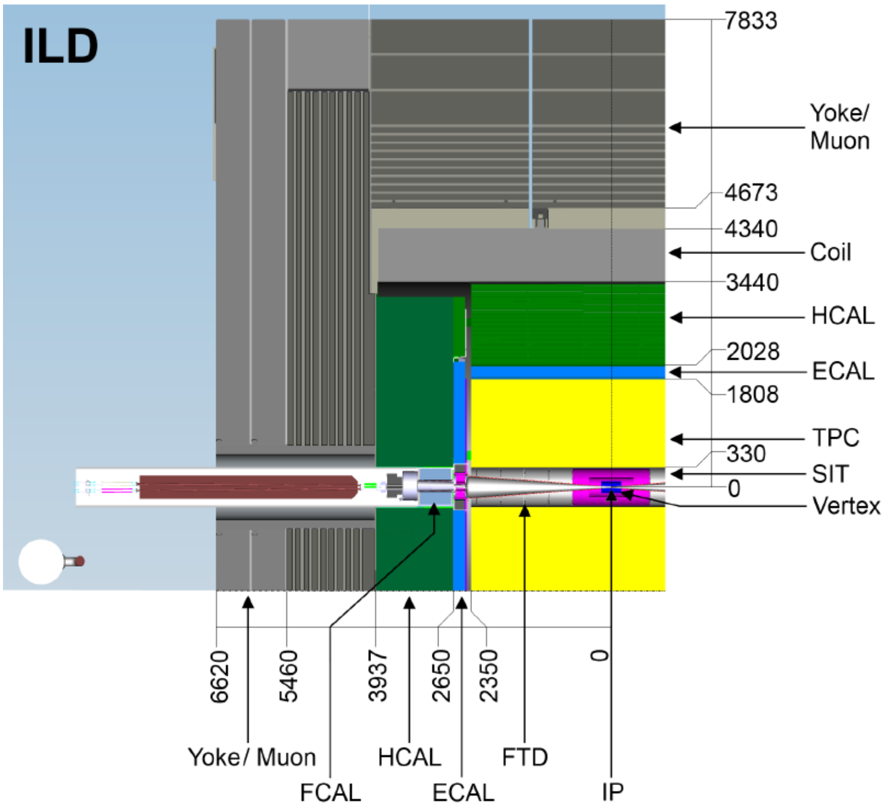

FIGURE 3.1: Cross sectional view of a quadrant of the ILD detector. The distance measures in mm.

Amongst all jet energies, 65% comes from charged particles, 27% from photons, 10% from neutral hadrons, and 1% from neutrinos. Moreover, up to a certain particle momentum (~100 - 150 GeV), the momentum resolution of tracking systems is more precise compared to the calorimeters. Therefore, for the calculation of the jet energy, PFA uses the tracker information for charged particles while using calorimeter information for others.

## 3.3 Tracking System

### 3.3.1 Vertex Detector

The inner most sub-detector of the ILD is the vertex detector (VXD). It consists of 3 cylindrical layers of pixel sensors, covering both surfaces of each layers. The main purpose of the VXD is to measure the interaction point by means of charge tracks. In addition it is designed to detect and measure the decay vertices of particles with longer lifetime that are fragmented from heavy quarks.. These particles have

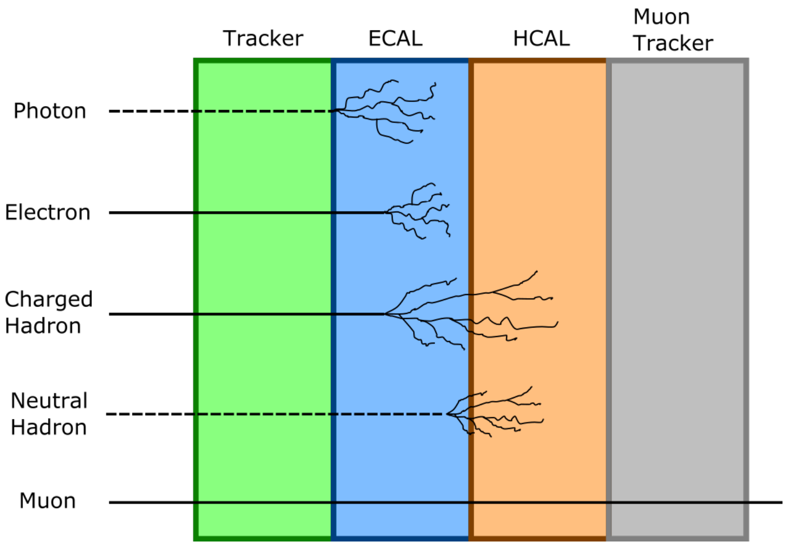

FIGURE 3.2: Schematic view of typical signal generation by final state particles issue of the $e^+e^-$ collision. .

relatively long lifetime which enable them to decay at the secondary vertex (SV) displaced away from the interaction point. As a result, identification of b and c quark is possible through the reconstruction of the SV. The impact parameter resolution required for the VXD is determined as below:

$$\sigma \leq 5 + \frac{10}{p\beta \sin^{3/2}\theta} \ (\mu m) \tag{3.1}$$

where $p$ is the momentum, $\beta$ is the velocity and $\theta$ is the polar angle for the incident particles. The first term 5 $\mu$m corresponds to the pixel size of the VXD and the second term originates from the multiple scattering which depends on the radiation length of the matters. Fig. 3.3 shows the schematic view of the VXD. It consists of three layers of the detectors, where each layer has pixel sensors on the both surfaces. The inner most layer is placed 16 mm above the collision point, thus this layer is constantly affected by the beam backgrounds. In order to resolve this issue, the number of pixels has been increased with multiple tests on their radiation resistance. Currently, pixel detectors such as CMOS and FPCCD are being considered as candidates to be mounted on the VXD.

### 3.3.2 Silicon Tracker

There are four types of silicon trackers located around the Time Projection Chamber (TPC). They are Silicon Inner Tracker (SIT), Silicon External Tracker (SET),

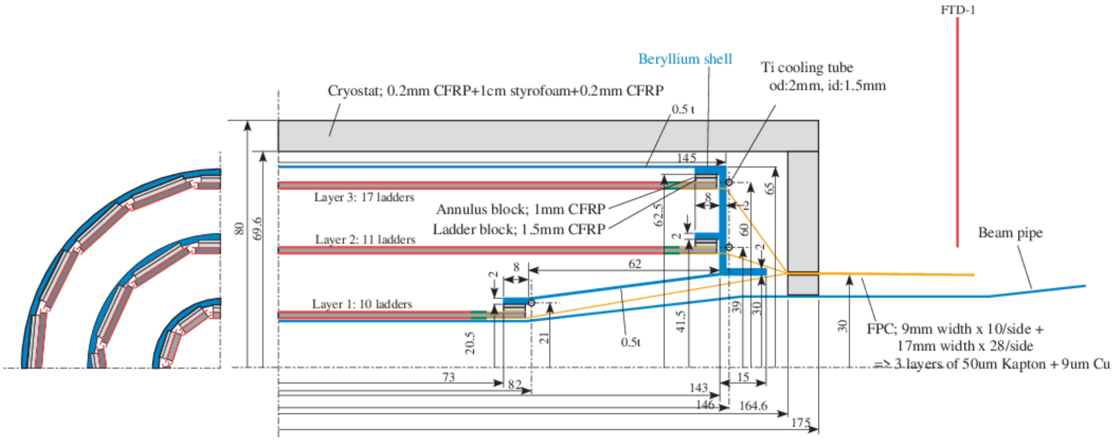

FIGURE 3.3: Schematic diagram of the VXD

Endplate of the TPC (ETD) and Forward Tracker (FTD). The configuration of each detector is shown in the Fig. 3.4. Silicon trackers are installed to assist the track reconstruction, enabling precise linking of the tracks measured with the TPC to the signals in the vertex detectors. as a result.

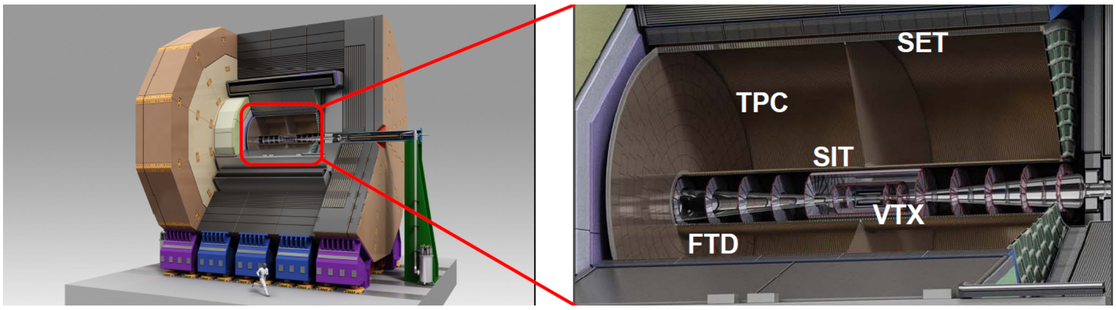

FIGURE 3.4: Configuration of silicon trackers

### 3.3.3 Time Projection Chamber

TPC is the central tracker of the ILD. As for the current baseline design, the gas chamber will be filled with T2K gas mixture (Ar-CF4(3%)-isobutane(2%) [9]) under the 3.5 T magnetic field in order to suppress the backgrounds. The TPC provides up to 220 3D points for each track associated to particles. In addition, the gas volume enables the particle identification from the dE/dx information and this new feature is exploited in this analysis. dE/dx is differential energy loss per unit length, and it can by approximated by Bethe formula

$$-\left\langle\frac{dE}{dx}\right\rangle = \frac{4\pi}{m_e c^2}\cdot\frac{nz^2}{\beta^2}\cdot\left(\frac{e^2}{4\pi\varepsilon_0}\right)^2\cdot\left[\ln\left(\frac{2m_e c^2\beta^2}{I\cdot(1-\beta^2)}\right)-\beta^2\right] \tag{3.2}$$

where $c$ is the speed of light, $\epsilon_0$ is the vacuum permittivity, $\beta$ is the velocity of the incident particle, $e$ is electric charge and $m_e$ is the mass of electron. Electron density $n$ can be calculated by

$$n = \frac{N_A \cdot Z \cdot \rho}{A \cdot M_u} \tag{3.3}$$

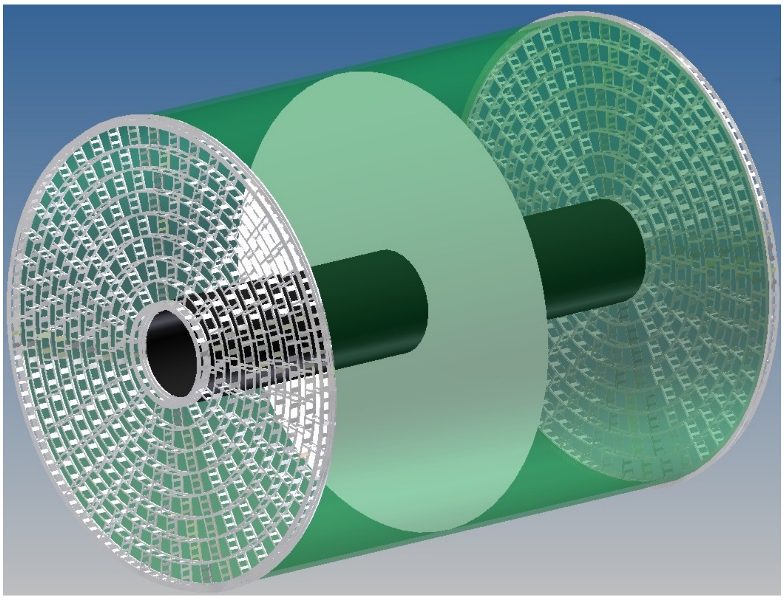

FIGURE 3.5: TPC design

# 3.4 Calorimeters

## 3.4.1 Electromagnetic Calorimeter

Electromagnetic calorimeter (ECAL) is placed outside of the TPC (Fig. 3.6). It consists of alternating layers of absorbers and detectors, and the main purpose is to achieve good particle separation while maintaining reasonable jet energy resolution. Typical energy resolution of the ILD calorimeters are in the order of $\sigma_E/E \sim 17\%/\sqrt{E/(GeV)}$ where $E$ is the whole jey energy range. ECAL design has to fulfill the following requirements:

- Separate the overlapping showers within the calorimeter.
- Reconstruct photons in the presence of the near-by charged particles.

- Extraction of detailed information from the shower (e.g. shower shape, starting point, energy etc.)

Both the electromagnetic and hadronic (see below) calorimeters are placed inside the magnetic coil, which supports the reconstruction of individual particles in the particle flow approach. Earlier study [10] suggests that tungsten is an appropriate material for the absorbers as it allows for a compact design and also since $\lambda_I/X_0 = 96mm/3.5mm$ is quite large it supports also the photon/hadron separation.

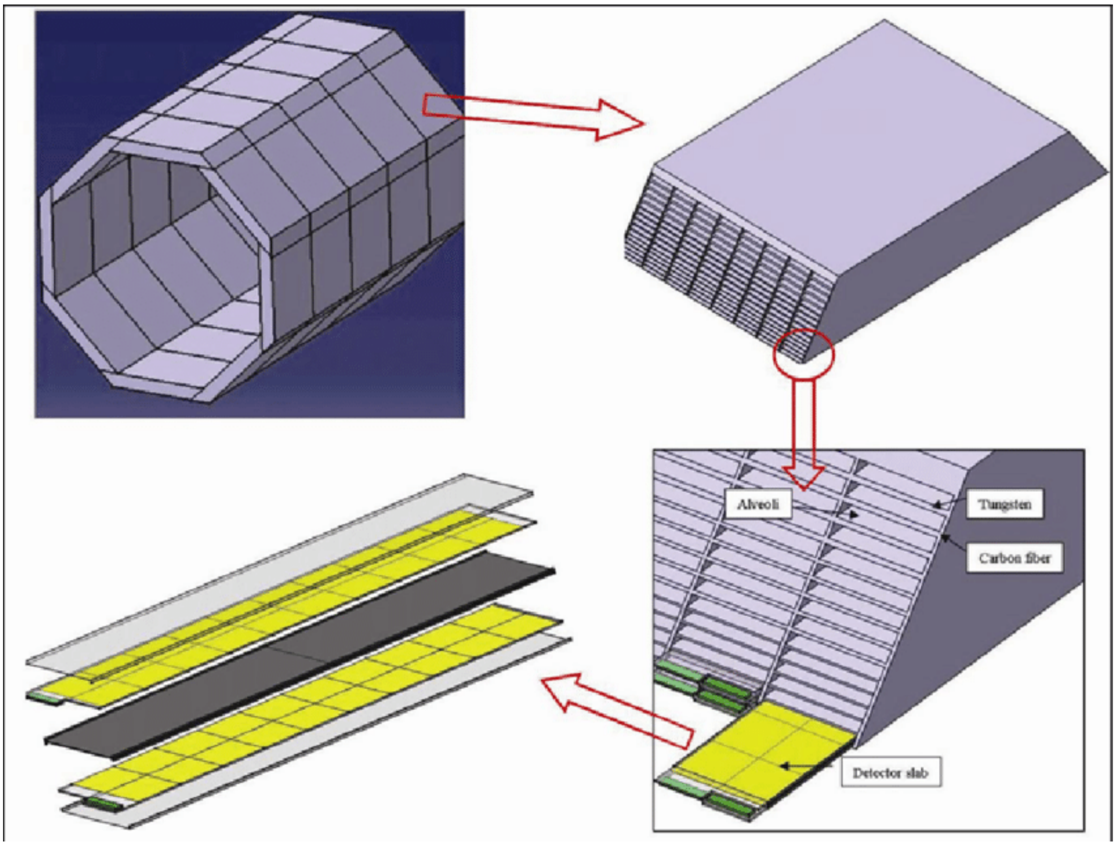

FIGURE 3.6: Cross section of the barrel part of the detection system. [1]

### 3.4.2 Hadronic Calorimeter

Hadrons deposit the largest fraction of their energy in the hadronic calorimeters, which has a typical depth of 5 $\lambda_I$. Calorimeters are the only way to measure neutral hadrons. Therefore the HCAL is of particular importance for this species. In order to measure its properties, it needs a good longitudinal sampling range while minimizing the detector volume. With all this, HCAL enables the particle reconstruction of neutral hadrons with the energy resolution of $\sigma_E/E \sim 50\%/\sqrt{E/(GeV)}$.

For the current baseline design, steel is considered as a good candidate for the absorber material. Steel has an interaction length of $\lambda_l = 17$ cm over radiation length $X_0 = 1.8$ cm.

### 3.4.3 Forward Calorimetry

There are two types of calorimeters foreseen to be mounted on the forward region of the ILD, namely BeamCal and LumiCal. The role of the LumiCal is to measure the luminosity with precision up to $10^{-3}$ at $\sqrt{s} = 500$ GeV, while BeamCal estimates the bunch-by-bunch luminosity, with an assist of a pair monitor, which is located next to the this.

## 3.5 Outer Detector

The sub-detectors so far are enclosed in the superconducting magnet if ILD. It creates a solenoidal magnetic field of up to 4 T parallel to the z-axis. The iron return yoke that shields the magnetic field to the outside can be be instrumented with either gaseous or scintillator detectors to optimise the muon detection or to act as a tail catcher for hadronic showers.

# Chapter 4

# Electroweak Coupling of Heavy Quarks in New Physics

In this thesis, the study of $e^+e^- \rightarrow t\bar{t}$ which is transmitted either $\gamma$ or $Z^0$ at $\sqrt{s} = 500$ GeV is presented. The Feynman diagram of this process is shown in Fig. 4.1 The study focuses on the interaction between $Z^0/\gamma$ and a top pair. This interaction is described by the form factors of the couplings, which is introduced in the chapter this chapter.

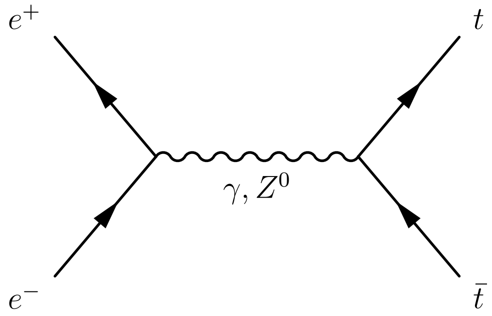

FIGURE 4.1: Feynman diagram top pair production.

## 4.1 Top Quark Property

Top quark is the heaviest quark in the Standard Model. The current world average of its mass is 173.07 GeV [7], which is 40 times larger than the mass of its partner quark, bottom quark, with a mass of about 4.5 GeV. This mass regime is comparable to the electroweak vacuum expectation value. Therefore, the precise measurements on the heavy quark properties play a central role for the indirect searches of the new particle beyond the Standard Model predictions to distinguish them from the various other theories.

Top quark decays via $t \to qW^+$ or $\bar{t} \to \bar{q}W^-$ process with $q = d, s, b$. Each down type quarks couples to top quark with coupling constant of $|g_{tq}|^2$.

| Channel | Decay Channel | Probability |
|---|---|---|
| Full Hadronic | $t\bar{t} \to b\bar{b}q\bar{q}'q\bar{q}'$ | 45.7% |
| Semi-leptonic | $t\bar{t} \to b\bar{b}\ \nu\bar{\ell}q\bar{q}'$ | 43.8% |
| Full leptonic | $t\bar{t} \to b\bar{b}\ \bar{\ell}\ell\nu\bar{\nu}$ | 10.5% |

Table 4.1: Top decay channel and decay ratio.

Table 4.1 indicates that the majority of top decay is dominated by semi-leptonic or full-hadronic channels. These couplings are determined by the Cabbibo-Kobayashi-Masukawa matrix [11, 12], also known as CKM matrix.

$$V_{CKM} = \begin{pmatrix} V_{ud} & V_{us} & V_{ub} \\ V_{cd} & V_{cs} & V_{cb} \\ V_{td} & V_{ts} & V_{tb} \end{pmatrix} = \begin{pmatrix} 0.974 & 0.225 & 0.00357 \\ 0.225 & 0.974 & 0.0411 \\ 0.00875 & 0.0403 & 0.999 \end{pmatrix} \tag{4.1}$$

where $|g_{qq'}|^2 = |V_{qq'}|^2 g_W^2$. When we look at the top couplings with each quarks, $|g_{tq}|^2$ becomes $|g_{td}|^2 \approx |g_{ts}|^2 \approx 0$ and $|g_{tb}|^2 \approx 1$. Thus the majority top quark decays through $t \to bW^+$ or $\bar{t} \to \bar{b}W^-$ process.

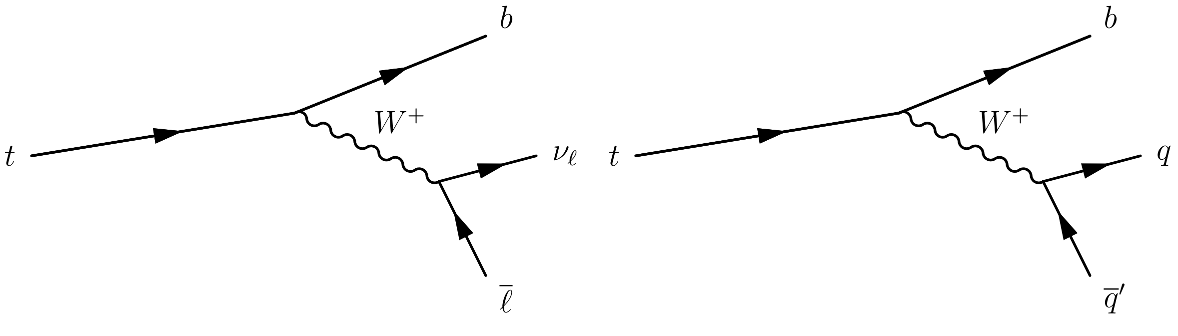

Figure 4.2: Feynman diagram of leptonically (left) and hadronically (right) decaying top

## 4.2 Electroweak Couplings of Top Quark

The vertex function describing the neutral vector boson interaction $X$ with a top pair can be expressed in terms of 10 form factors. The current at the decay vertex at $t\bar{t}X$, where $X$ is $Z^0$ or $\gamma$ can be deduced from the current at the ffZ vertex, which can be expressed in terms of vector and axial form factors, $F^X_{1,2V}$ and $F^X_{1,2A}$. Using the Gordon decomposition, eq. **??** can be rewritten in the following format for on-shell top quarks:

$$\Gamma^{t\bar{t}X}_{\mu}(k^2,q,\bar{q}) = ie\left[\gamma_\mu\left(\tilde{F}^X_{1V}(k^2)+\gamma_5\tilde{F}^X_{1A}(k^2)\right)+\frac{\sigma_{\mu\nu}}{2m_t}(q+\bar{q})^\nu\left(i\tilde{F}^X_{2V}(k^2)+\gamma_5\tilde{F}^X_{2A}(k^2)\right)\right] \tag{4.2}$$

where $k^2$ is the four-momentum of the interacting boson, $q$ and $\bar{q}$ are the four vectors of $t$ and $\bar{t}$. $\sigma_{\mu\nu} = \frac{i}{2}(\gamma_\mu\gamma_\nu - \gamma_\nu\gamma_\mu)$ and those form factors are

$$\begin{cases} \tilde{F}^X_{1V} & = -(F^X_{1V}+F^X_{2V}) \\ \tilde{F}^X_{2V} & = F^X_{2V} \\ \tilde{F}^X_{1A} & = -F^X_{1A} \\ \tilde{F}^X_{2A} & = -iF^X_{2A} \end{cases} \tag{4.3}$$

Then, the Standard Model form factors for each bosons have following values:

$$\begin{cases} F^\gamma_{1V} & = \frac{2}{3} \\ F^\gamma_{1A} & = 0 \\ F^Z_{1V} & = \frac{1}{\cos\theta_W\sin\theta_W}(1-\frac{8}{3}\sin^2\theta_W) \\ F^Z_{1A} & = -\frac{1}{4\cos\theta_W\sin\theta_W} \end{cases} \tag{4.4}$$

$F^X_{2V,A}$ are the form factors related to magnetic and electric dipole moment, respectively.

## 4.3 Matrix Element Calculation

### 4.3.1 Top Pair Production

One can analyze the top quark decay process as a sequence of three processes. $e^-e^+ \to t\bar{t}$, $t \to bW^+$ and $W^+ \to \bar{\ell}\nu$. The scattering amplitude is the correlation of matrix elements for each process.

$$\left|\sum_{\eta\eta',\lambda\lambda',\rho\rho'} \mathcal{M}(e^-_\sigma e^+_{\sigma'} \to t_\eta \bar{t}_{\eta'})\mathcal{M}(t_\eta \to b_\rho W^+_\lambda)\mathcal{M}(\bar{t}_{\eta'} \to \bar{b}_{\rho'} W^-_{\lambda'})\mathcal{M}(W^+_\lambda \to \bar{\ell}\nu)\mathcal{M}(W^-_{\lambda'} \to \ell\nu)\right|^2 \tag{4.5}$$

where $\sigma, \eta, \lambda, \rho$ represents the initial state of helicities. The matrix element for the decay vertex of $e^-e^+ \to t\bar{t}$, in terms of form factors is shown below.

$$i\mathcal{M}^{X\mu} = ie\left(\gamma^\mu[F^X_{1V} + F^X_{1A}\gamma_5] + \frac{i\sigma^{\mu\nu}q_\nu}{2m_t}[F^X_{2V} + F^X_{2A}]\right) \tag{4.6}$$

The values of form factors in Standard Model at the tree level is stated in eq. 4.4. Form factors with polarized beam can be expressed in polarization state of incident electron [13]

$$\begin{cases} \mathcal{F}^L_{ij} & = -F^\gamma_{ij} + \left(\frac{-\frac{1}{2}+\sin^2\theta_W}{\sin\theta_W\cos\theta_W}\right)\left(\frac{s}{s-m_Z^2}\right)F^Z_{ij} \\ \mathcal{F}^R_{ij} & = -F^\gamma_{ij} + \left(\frac{\sin^2\theta_W}{\sin\theta_W\cos\theta_W}\right)\left(\frac{s}{s-m_Z^2}\right)F^Z_{ij} \end{cases} \tag{4.7}$$

where $i = 1, 2$ and $j = V, A$. Calculation of each matrix element with different polarization combination were performed. We defined $\theta$ ($\phi$) to be the top polar (azimuthal) angle respect to the electron beam direction. (Fig. 4.3)

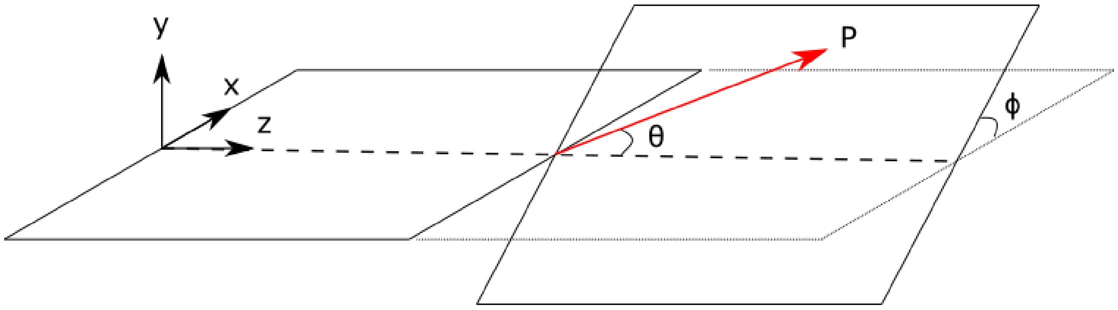

Figure 4.3: Angular definition

Each fermions has spin $\frac{1}{2}$ and their helicities are $\lambda = \pm\frac{1}{2}$.

$$\begin{aligned}
\mathcal{M}(e^-_L e^+_R \to t_L \bar{t}_R) &= (\mathcal{F}^L_{1V} - \beta\mathcal{F}^L_{1A} + \mathcal{F}^L_{2V})(1+\cos\theta)e^{-i\phi} \\
\mathcal{M}(e^-_L e^+_R \to t_R \bar{t}_L) &= (\mathcal{F}^L_{1V} + \beta\mathcal{F}^L_{1A} + \mathcal{F}^L_{2V})(1-\cos\theta)e^{-i\phi} \\
\mathcal{M}(e^-_L e^+_R \to t_L \bar{t}_L) &= \gamma^{-1}(\mathcal{F}^L_{1V} + \gamma^2(\mathcal{F}^L_{2V} + \mathcal{F}^L_{2A}))(\sin\theta)e^{-i\phi} \\
\mathcal{M}(e^-_L e^+_R \to t_R \bar{t}_R) &= \gamma^{-1}(\mathcal{F}^L_{1V} + \gamma^2(\mathcal{F}^L_{2V} - \mathcal{F}^L_{2A}))(\sin\theta)e^{-i\phi} \\
\mathcal{M}(e^-_R e^+_L \to t_L \bar{t}_R) &= -(\mathcal{F}^R_{1V} - \beta\mathcal{F}^R_{1A} + \mathcal{F}^R_{2V})(1+\cos\theta)e^{i\phi} \\
\mathcal{M}(e^-_R e^+_L \to t_R \bar{t}_L) &= -(\mathcal{F}^R_{1V} + \beta\mathcal{F}^R_{1A} + \mathcal{F}^R_{2V})(1-\cos\theta)e^{i\phi} \\
\mathcal{M}(e^-_R e^+_L \to t_L \bar{t}_L) &= \gamma^{-1}(\mathcal{F}^R_{1V} + \gamma^2(\mathcal{F}^R_{2V} + \mathcal{F}^R_{2A}))(\sin\theta)e^{i\phi} \\
\mathcal{M}(e^-_R e^+_L \to t_R \bar{t}_R) &= \gamma^{-1}(\mathcal{F}^R_{1V} + \gamma^2(\mathcal{F}^R_{2V} - \mathcal{F}^R_{2A}))(\sin\theta)e^{i\phi}
\end{aligned} \tag{4.8}$$

where $\beta^2 = 1 - \frac{4m_t^2}{s}$ and $\gamma = \frac{\sqrt{s}}{2m_t}$. From eq. 4.8, one can determine the angular dependence of each process with scattering amplitudes.

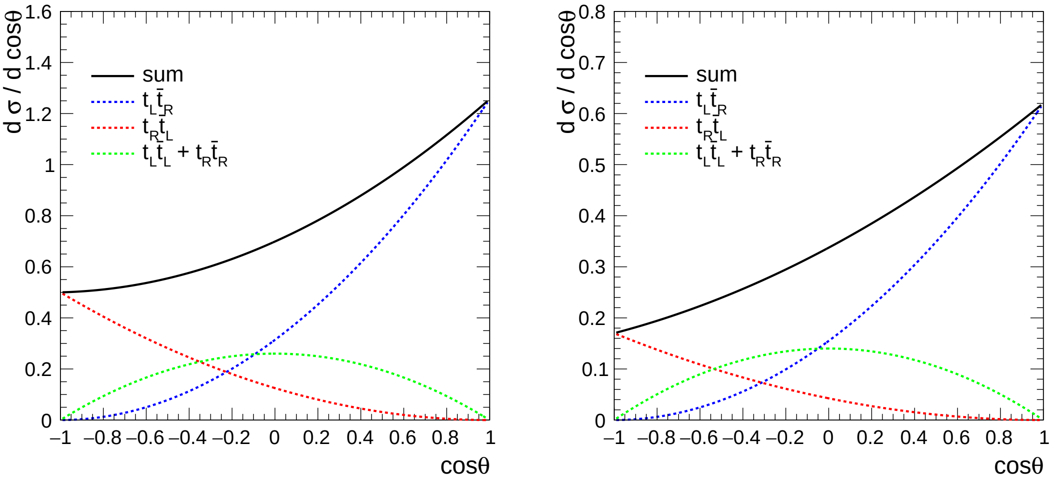

FIGURE 4.4: Differential cross section of $e^-e^+ \to t\bar{t}$ plotted against the polar angle of left handed (*left*) and right handed (*right*) top quarks.

Fig. 4.4 shows the differential cross section of top quarks. This quantity will be experimentally verified in the chapter 7.

### 4.3.2 Top decay

In the section 1.3.2, we have seen that the coupling between two fermions and weak vector bosons follows a V-A structure. In fact, decay amplitude of such interaction can be written in terms of form factors:

$$i\mathcal{M}^{W\mu} = i\frac{g}{\sqrt{2}}\left(\gamma^\mu[F^W_{1L}P_L + F^W_{1R}P_R] + i\frac{\sigma^{\mu\nu}q_\nu}{2m_t}[F^W_{2L}P_R + F^W_{2R}P_L]\right) \tag{4.9}$$

where $P_{R,L}$ is the chiral projection operator and defined as

$$P_{R,L} = \frac{1 \pm \gamma_5}{2} \tag{4.10}$$

The helicity $L$ and $R$ are chosen so that it matches with outgoing $b$ helicity. In this study, the limiting case of $m_b = 0$ was assumed to reduce the parameters $F^W_{1R} = F^W_{2R} = 0$. At the tree level Standard Model, $F^W_{1L} = 1$.

After boosting the frame of reference from lab to the top quark, one can compute the matrix elements in this frame. For the helicity angles, $\theta_W$ and $\phi_W$ are the polar and azimuthal angle of W boson with respect to the top flight direction.

$$\begin{aligned}
\mathcal{M}(t_R \to b_L W^+_0) &= \left(\frac{m_t}{m_W}F^W_{1L} - \frac{m_W}{2m_t}F^W_{2L}\right)\left(\cos\frac{\theta_W}{2}\right)e^{i\phi_W} \\
\mathcal{M}(t_L \to b_L W^+_0) &= \left(\frac{m_t}{m_W}F^W_{1L} - \frac{m_W}{2m_t}F^W_{2L}\right)\left(\sin\frac{\theta_W}{2}\right)e^{-i\phi_W} \\
\mathcal{M}(t_R \to b_L W^+_L) &= \sqrt{2}\left(F^W_{1L} - \frac{1}{2}F^W_{2L}\right)\left(-\sin\frac{\theta_W}{2}\right)e^{i\phi_W} \\
\mathcal{M}(t_L \to b_L W^+_L) &= \sqrt{2}\left(F^W_{1L} - \frac{1}{2}F^W_{2L}\right)\left(\cos\frac{\theta_W}{2}\right)e^{-i\phi_W}
\end{aligned} \tag{4.11}$$

Here, the factor of $\frac{igm_t\sqrt{1-\left(\frac{m_W}{m_t}\right)^2}}{\sqrt{2}}$ is dropped. Note that due to the conservation of angular momentum, $\mathcal{M}(t_L \to b_L W^+_R) = \mathcal{M}(t_R \to b_L W^+_R) = 0$. In order to obtain the matrix elements of right handed case, one only needs to switch following variables, $L \leftrightarrow R$, $\theta_t \leftrightarrow -\theta_t$ and $\phi_t \leftrightarrow -\phi_t$.

### 4.3.3 Cross Section

Eq. 4.7 defined the form factors in terms of the helicity of the electron and positron beams. Then the cross section of top pair production with beam polarization $I = L, R$ is derived as

$$\sigma_I = 2\left(\frac{4\pi\alpha^2}{3s}\right)N_c\beta\left[\left(1+\frac{1}{2\gamma^2}\right)(F^I_{1V})^2 + (\beta F^I_{1A})^2 + 3F^I_{1V}F^I_{2V}\right] \tag{4.12}$$

where $\alpha$ is the electromagnetic coupling constant, $N_c$ is the number of quark colors, $\gamma$ is the Lorentz factor and $\beta$ is velocity. ILC is capable of controlling the beam polarization at the beginning, which gives the robust description of the initial states of electron and positrons. Nevertheless, full polarization is not possible in the realistic scenario. Thus polarization of electron and positron are expressed as $\mathcal{P}_{e^-}$ and $\mathcal{P}_{e^+}$, respectively. Then the cross section of any process at the ILC with these polarization is expressed as:

$$\sigma_{\mathcal{P}_{e^-},\mathcal{P}_{e^+}} = \frac{1}{4}[(1-\mathcal{P}_{e^-}\mathcal{P}_{e^+})(\sigma_{L,R}+\sigma_{R,L}) + (\mathcal{P}_{e^-}-\mathcal{P}_{e^+})(\sigma_{R,L}-\sigma_{L,R})] \tag{4.13}$$

### 4.3.4 Forward Backward Asymmetry and Form Factors

The fact that ILC can manipulate the polarization of the beam at the real experiment enables us to extract forward and backward asymmetry both from the theory and experimental observables. Using form factors from eq. 4.7, we obtain the forward backward asymmetry as:

$$(A^t_{FB})_I = \frac{-3\beta F^I_{1A}(F^I_{1V}+F^I_{2V})}{2[(1+\frac{1}{2\gamma^2})(F^I_{1V})^2 + (\beta F^I_{1A})^2 + 3F^I_{1V}F^I_{2V}]} \tag{4.14}$$

In the Standard Model, this value takes [10]

$$(A^t_{FB})_L = 0.38 \quad (A^t_{FB})_R = 0.47 \tag{4.15}$$

# Chapter 5

# Event Selection

In this chapter, a full simulation study of top pair production $\sqrt{s} = 500$ with a recent model of ILD that was also used for the Intermediate Design Report (IDR) of ILD, followed by both semi-leptonic and full-hadronic top pair reconstruction process are presented. The actual reconstruction of the two processes share a number of commonalities. A notable difference is the presence of the isolated lepton in case of the semi-leptonic channel. The analysis techniques for both channel are described in Chapter 7.

After the pair production, top quarks decay via full-leptonic, semi-leptonic and full-hadronic as described in section 4.1. Fig. 5.1 shows a sketch of the top pair decay process. For the semi-leptonic process, leptonically (hadronically) decaying top is labeled top1 (top2). For the full-hadronic process, the top with the highest b-tag value (see Sec. 5.4.3) is labeled top1 and second highest is labeled top2. For the differential cross section, the analysis has to be able to distinguish between top and anti-top. There are three important key parameters to measure in this study: vertex charge, kaon charge and isolated lepton charge (only for semi-leptonic channel). In order to measure these parameters, it is necessary to precisely reconstruct b-jets and isolated lepton.

## 5.1 Event Generator

For the signal and background generation, WHIZARD [14, 15] ver 1.95 is used. WHIZARD is the program to calculate the cross section for the multi-scattering process up until NLO for both QCD and QED interactions. $e^+e^- \to b\bar{b}\ell\nu q\bar{q}'$ and $e^+e^- \to b\bar{b}q\bar{q}'q\bar{q}'$ samples in which dominated by top pair production events were used. The samples also contain single top events with the same final states and this is analyzed in Chapter 6.3. The integrated luminosity of 2200 fb$^{-1}$ is available for each polarization yet final state of $W \to \tau\nu_\tau$ was excluded for the sake of simplifying the analysis. WHIZARD is the interface for the PYTHIA 6.4 [16] which is used for parton shower hadronization.

## 5.2 Detector Simulation

GEANT4 was used for the detector simulations and the detector geometry is provided by the software interface called DD4Hep [17]. The simulated energy depositions are further digitized for a realistic approximation of the detector response.

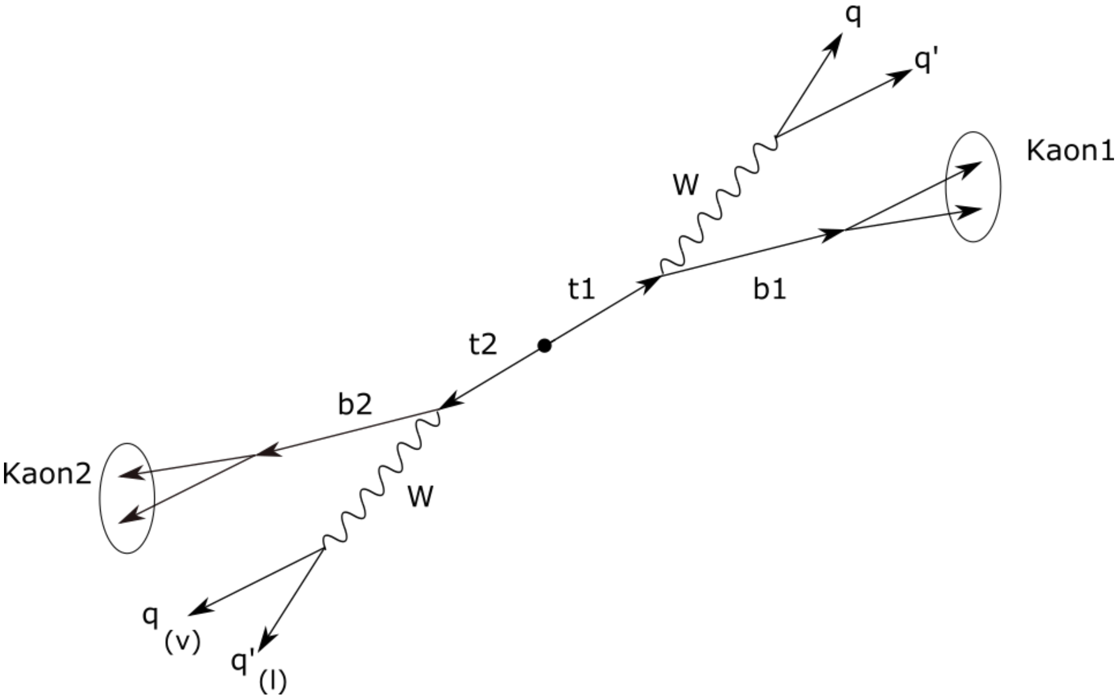

Figure 5.1: Sketch of top quark pair decay process.

## 5.3 Isolated Lepton Finder

Identifying the isolated lepton from the W decay is the first step of the event reconstruction. It is necessary to remove the isolated lepton from the list of PFOs before the jet reconstruction.

The algorithm to find the isolated lepton is implemented in the processor called *IsolatedLeptonTagging* [18] of iLCSoft. There are three steps to complete the process.

- *Energy/momentum selection* The W decays into high energetic leptons. The processor selects electron/muon with $P > 5$ GeV. Then it examines the correlation between energies deposited in ECAL (HCAL), $E_{ecal}$ ($E_{hcal}$), and the sum of both, $E_{tot}$. For electrons, it is required to be $E_{ecal}/E_{tot} > 0.9$ and $0.5 < E_{tot}/P < 1.3$. For muons, it is required to be $E_{ecal}/E_{tot} < 0.3$ and $E_{yoke} > 1.2$ GeV.
- *Impact parameter* : Electron/muon is required to have impact parameters consistent with the one from the primary vertex (PV). The method used to measure this impact parameter is shown in the section 5.4.1.
- *Cone* is defined around electron/muon candidates. The sum of energies deposited within the cone from charged and neutral particles is then computed. The input criteria of parameters to isolate lepton are defined in the Toolkit for Multivariate Analysis (TMVA).

## 5.4 Jet Reconstruction

After removing the isolated lepton from the list of PFOs, LCFIPlus [19] reconstructs primary and secondary vertices, and tags the flavors of jets associated to them. Generalized $k_T$ algorithm for $e^+e^-$ collisions [**?** ] was used for jet clustering, and Valencia algorithm was used to remove $\gamma\gamma$ backgrounds.

### 5.4.1 The LCFIPlus Package

The LCFIPlus package is implemented within the framework of Marlin processors, and its purpose is to tag heavy flavor jets. Its algorithm is established upon another package called LCFIVertex [21], which was originally developed to tag the vertices corresponding to the flavor tagged jets for Z-pole physics. Unlike the LCFIVertex, LCFIPlus reconstructs PV and SV prior to the reconstruction of the jets to facilitate usage of vertex information upon jet reconstruction. After the jet reconstruction, TMVA is used to specifies the selection parameters for the flavor tagging of the jets. The steps to reconstruct jets are shown below:

- PV is determined using fit with $\chi^2$ minimization method, which uses all charged tracks from the expected beam spot. After applying the cut in the $\chi^2$ values, those tracks did not satisfy its condition is removed.
- SV is reconstructed based on the PV information. First the algorithm looks for any combinations of tracks that is not associated to PV and forms seeds to SV. Then the $\chi^2$ value is computed for each combinations. Invariant mass of combined track pairs must be smaller than the energy of both tracks or threshold value. The $\chi^2$ value must also be smaller than the threshold value.

### 5.4.2 Jet Clustering

After the vertex identification, the particle flow objects are clustered into jets within LCFIplus using the Durham algorithm. The vertices identified in the previous step serve as cores for the jet finding. In the generalized $k_T$ algorithm for $e^+e^-$ collisions, it first computes the two following distances:

$$d_{ij} = \min(E_i^2, E_j^2)\frac{(1-\cos\theta_{ij})}{(1-\cos R)} \tag{5.1}$$

$$d_{iB} = E_{iB}^2 \tag{5.2}$$

where $\theta_{ij}$ is the separation angle of two jets, $E_{i,j}$ is the energies of each object, and $R$ is the cone radius which is defined to be 1.5 for this analysis. At the each stage of the clustering process, if $d_{ij}$ is the smallest, then object $i$ and $j$ are combined. When $d_{iB}$ is the smallest, $i$ itself becomes a jet. The performance of this jet clustering method is evaluated in Ref. [22]. In a last step the tracks associated to PFO within a jet with secondary vertices are reanalysed and assigned to vertices if appropriate.

### 5.4.3 b-Tagging

The likeliness of a jet containing a b-quark is called b-tag. Hadrons which include b quark have mean lifetime of $\sim 10^{-12}$ s. They decay thus at distances of c$\tau$ 450$\mu$m from the primary vertex yielding a well-measurable secondary vertex. The flavor tagging input variables are constructed from the constituents of the jets such as the charged tracks and secondary vertices and the resulting b-tag parameter takes values between 0 and 1. Vertex detectors in the ILD enable an efficient flavor tagging with fine resolution. Figure 5.2 shows b-jet momentum distribution with semi-leptonic and full-hadronic scenario. This indicates the b-tag performance for the jet reconstruction would not be dependent on the decay channels.

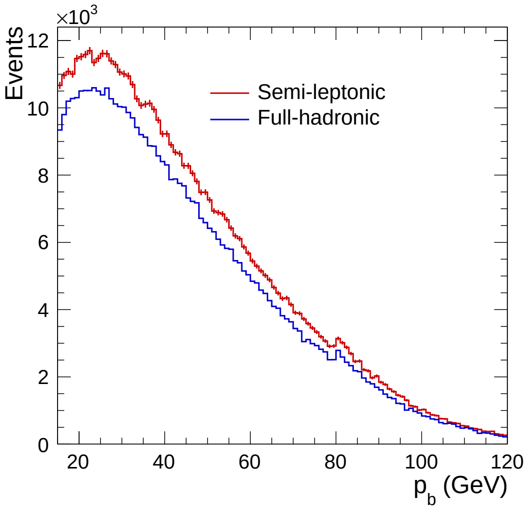

FIGURE 5.2: Momentum of reconstructed b-jets

## 5.5 Vertex Recovery

In the pre-studies [23], it is said that the vertex reconstruction algorithm starts to lose their efficiency at below an average prong momentum of 4 GeV. Further reasons why vertex reconstruction fails are:

- *Soft B hadrons* with low energies will decay not far from the interaction point, which makes it difficult to separate its offsets from the primary vertex.
- *A one prong decay vertex* will not be reconstructed.
- *Detector acceptance* A limited detector acceptance results in a track loss and compromises therefore the vertex reconstruction.

The vertex recovery algorithm identifies the reconstructed tracks that have not been associated to secondary vertices from B-Meson decays. The vertex recovery algorithm uses the offset significance to recover vertices.

$$\epsilon/\sigma = \left|\frac{d_0}{\sigma_{d_0}}\right| + \left|\frac{z_0}{\sigma_{z_0}}\right| \tag{5.3}$$

where the definition of $d_0$ and $z_0$ are illustrated in the fig. 5.3. $\sigma_{d_0}$ and $\sigma_{z_0}$ are the

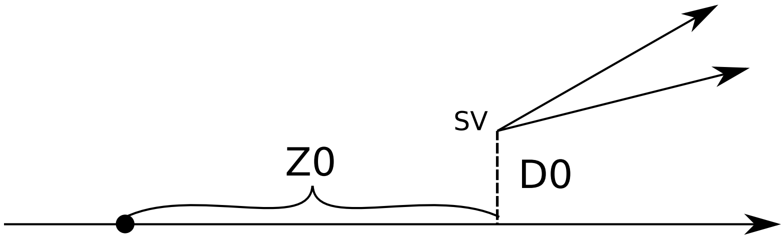

FIGURE 5.3: Illustration of the secondary vertex distance.

covariance matrix elements provided by the PFA.

Fig. 5.4 show the missed tracks before and after vertex recovery for the $e^+e^- \rightarrow t\bar{t}$ analyses, respectively. Both figures suggest that the number of missed tracks are lower for after the vertex recovery.

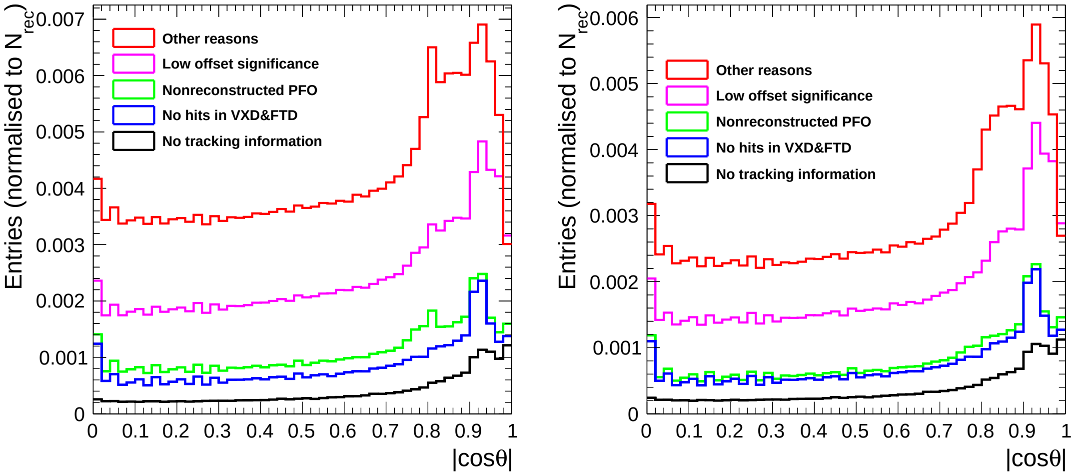

FIGURE 5.4: Polar angle distribution of missed tracks before (left) and after (right) the vertex recovery.

In Fig. 5.5, the reconstructed b charge purity is plotted against b-tag, B hadron momentum, number of reconstructed prongs belonging to the b vertex, and polar angle of the B hadron with respect to the beam direction. The charge purity $p_b$ is defined as:

$$p_b = \frac{N_{corr.}}{N_{total}} \tag{5.4}$$

where $N_{corr.}$ ($N_{total}$) is the number of correctly (total) reconstructed b quark charge.

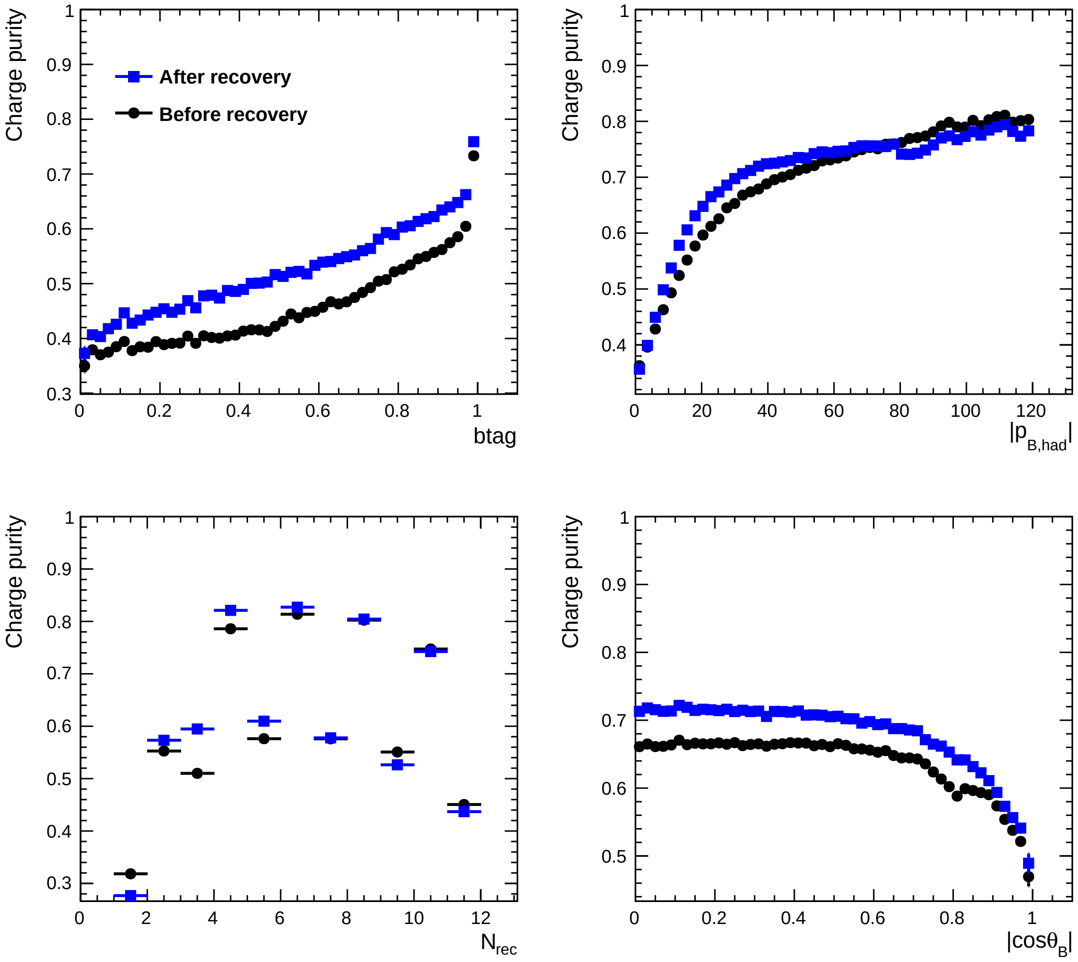

FIGURE 5.5: b charge purity before and after the vertex recovery with different physical parameters.

From these plots, we can draw four conclusions:

- Vertex recovery improves reconstructed b charge purity throughout the entire b-tag spectrum. The b-tag value is sensitive to the offsets of reconstructed prongs. When b-tag is low, jet will have less offsets which makes it difficult to recover prongs.
- Improvement can be seen for the jets with low number of reconstructed prongs, especially with $N_{rec} = 3$.
- Vertex recovery algorithm can successfully reconstruct b charge even at the edge of the barrel of VXD, which happens at $|\cos\theta_B| \approx 0.8$.

## 5.6 Kaon Identification

82% of $B$ mesons decay to kaons with right charge. Thus charge of kaon reflects the charge of underlying $b$ quark. While vertex charge information contributes to the reconstruction of a $b$ charge, it is also essential to use the kaon charges, which decayed from the $b$, in order to have additional candidates of charge to reconstruct top quark in the end. This is effective particularly in case of full hadronic channel, since it cannot rely on isolated lepton charge information.

### 5.6.1 dE/dx Information

In order to reconstruct charged kaon $K^{\pm}$, $dE/dx$ information measured in the TPC is used. $dE/dx$ is the energy deposited inside the TPC per differential distance. The mass region of kaon resides above pion, below proton. $dE/dx$ depends on the velocity of the particle, thereby for a given momentum, dE/dx depends on the mass. Therefore, kaon can be identified through $dE/dx$ information.

Fig. 5.6 shows the projection of $dE/dx$ between the momentum range on the title. This indicates the minimum of 2 GeV is required to separate the kaons from the other particles. Then, the distribution of $dE/dx$ plotted against the particle momentum is shown in the Fig. 5.7. Green, red and blue data points represent proton, kaon and pions, respectively. Each particles is identified by using particle likelihood by comparing with generated information.

## 5.7 Chi-2 Minimization

Chi-2 minimization is a technique developed to reconstruct particles with clearer identification of b jets and W boson combinations for top quark reconstruction, and quark jets combination for hadronic W reconstruction.

For reconstructing top quarks, $\chi^2_{top}$ quantity is determined as equation below:

$$\chi^2_{top} = \left(\frac{m_t - 174}{\sigma_{m_t}}\right)^2 + \left(\frac{E_t - 250}{\sigma_{E_t}}\right)^2 + \left(\frac{p_b^* - 68}{\sigma_{p_b^*}}\right)^2 + \left(\frac{\cos\theta_{Wb} - 0.23}{\sigma_{\cos\theta_{Wb}}}\right)^2 + \left(\frac{\gamma_t - 1.435}{\sigma_{\gamma_t}}\right)^2 \tag{5.5}$$

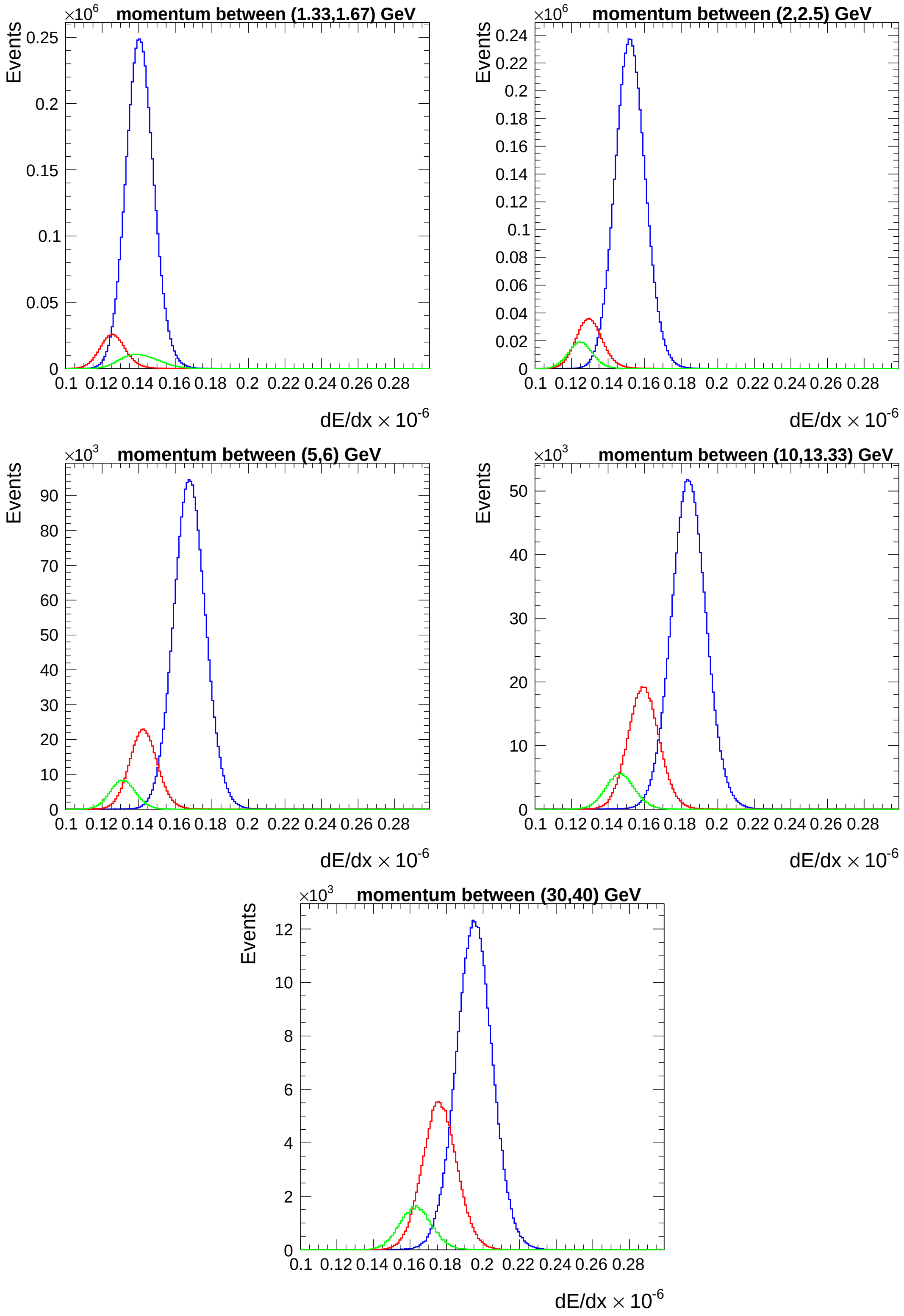

FIGURE 5.6: Projection of dE/dx plot against different momentum range

where $m_t$, $E_t$, and $\gamma_t$ are mass, energy and Lorentz gamma for reconstructed top, respectively. $p_b^*$ is the momentum of b jet in top frame and $\theta_{Wb}$ is the separation angle between W and b. Eq. 5.5 minimizes the $\chi^2_{top}$ around the expected values of

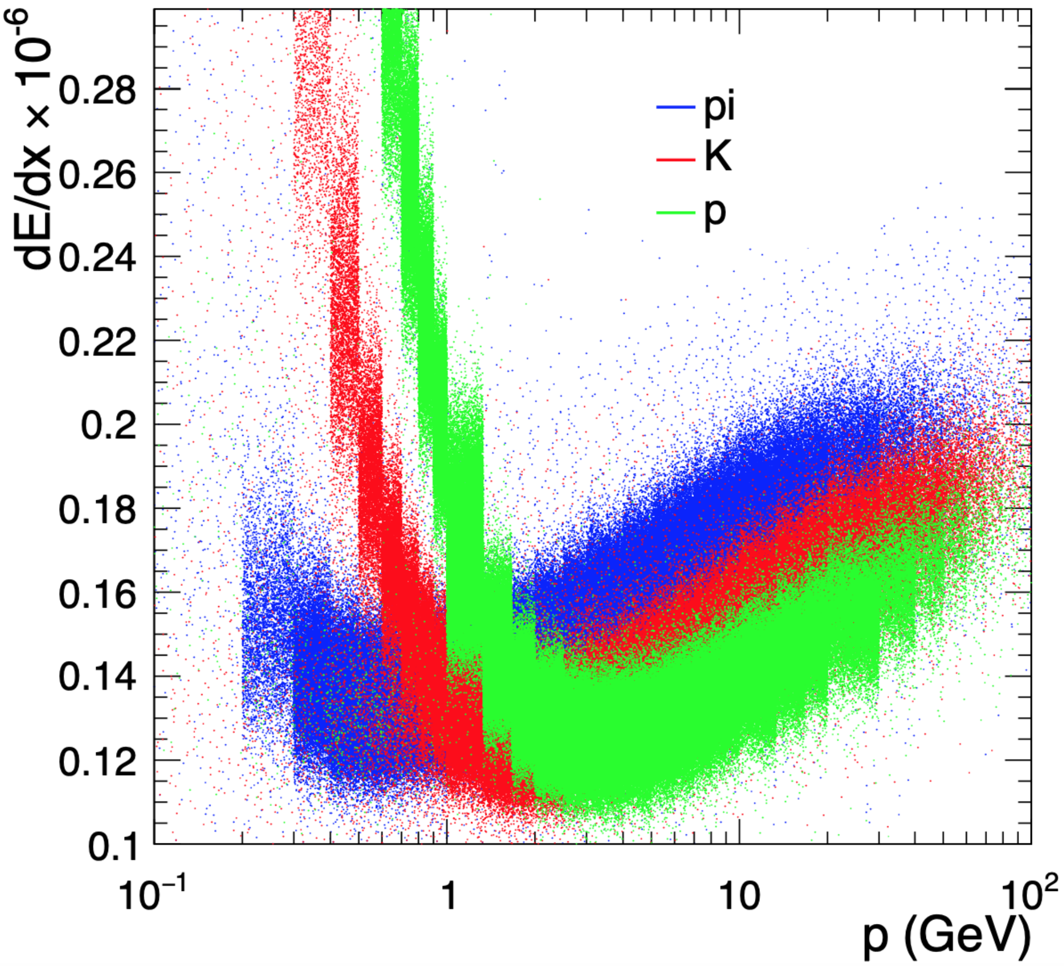

Figure 5.7: dE/dx plotted against momentum.

the corresponding physical variables. Fig. 5.8 is the computation result for the $\chi^2$ with semi-leptonic and full-hadronic channel. In this analysis, the cut of $\chi^2 < 30$ is applied to reject the background emerges from the mis-combination of $b$ and W.

$\chi^2_W$ is required to reconstruct hadronic Ws in full-hadronic channel.

$$\chi^2_W = \left( \frac{m_W - 80.3}{\sigma_{m_W}} \right)^2 \tag{5.6}$$

## 5.8 Top Quark Reconstruction

In this thesis, semi-leptonic and full-hadronic channel of the $t\bar{t}$ decays are analyzed.

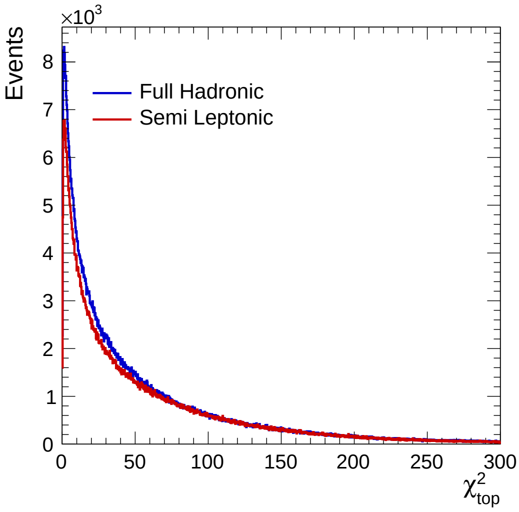

FIGURE 5.8: $\chi^2_{top}$ distribution for reconstructing of top

### 5.8.1 Semi-leptonic Channel

In the semi-leptonic case, final state is composed of 4 jets and 1 lepton. In order to reconstruct the top, it is essential to associate hadronic decaying W with one of the two $b$'s. The distinction between $t$ and $\bar{t}$ either happen with charge of the lepton or charge of the b's. Event selection and its efficiencies are presented in the table 5.2.

$e^- e^+ \to t\bar{t} \to b\bar{b}\ell\nu q\bar{q}'$ at 500 GeV

| | $e^-_L e^+_R$ | $e^-_R e^+_L$ |
|---|---|---|
| Isolated Lepton | 95.1% | 94.1% |
| $btag_1 > 0.8$ or $btag_2 > 0.3$ | 83.9% | 84.9% |
| Thrust $< 0.9$ | 83.9% | 84.9% |
| Hadronic mass | 80.8% | 82.2% |
| Reconstructed $m_W$ and $m_t$ | 75.8% | 77.6% |

TABLE 5.1: Event selection efficiencies after each preselection criteria for semi-leptonic process.

Since leptonically decaying W contains neutrino as a final state, energy for the leptonic top / W cannot be determined. Thus the mass of the hadronic W and top are first reconstructed, followed by the recoil mass reconstruction of leptonic top. Mass distribution of hadronic and leptonic W / top are shown in the Fig. 5.9. $L$ and $R$ represent the polarization of the beam.

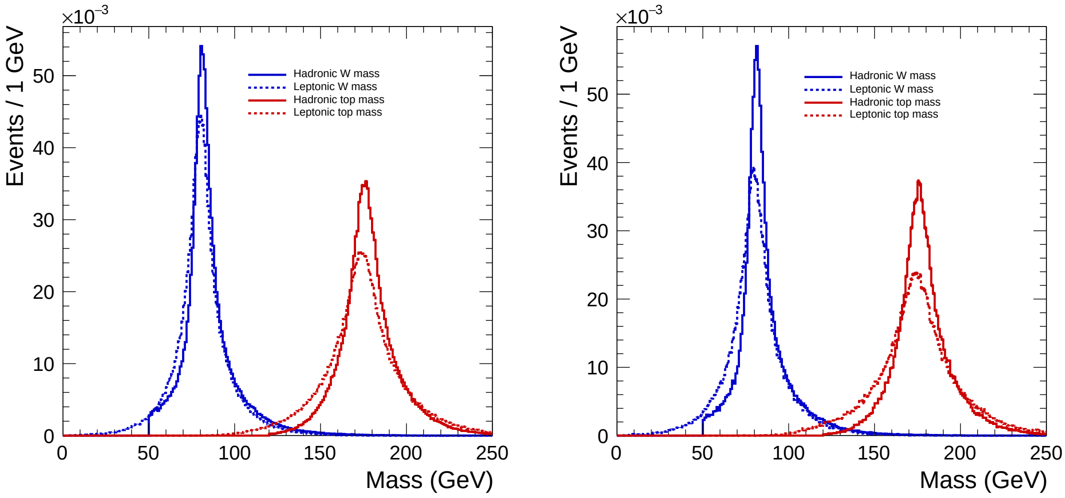

Figure 5.9: Reconstructed invariant mass distributions of $e^-_L e^+_R$ (left) and $e^-_R e^+_L$ (right) in semi-leptonic channel.

### 5.8.2 Full-hadronic Channel

In the full-hadronic case, final state is composed of 6 jets. Nevertheless the number of possible combination is higher, as one needs to associate 2 b-jets with 4 W jets.and the distinction between $t$ and $\bar{t}$ can only happen via the charge of b's.

$e^-e^+ \to t\bar{t} \to b\bar{b}q\bar{q}'q\bar{q}'$ at 500 GeV

| | $e^-_L e^+_R$ | $e^-_R e^+_L$ |
|---|---|---|
| $btag_1 > 0.8$ or $btag_2 > 0.3$ | 72.1% | 71.4% |
| Thrust $< 0.9$ | 72.1% | 71.4% |
| Hadronic mass | 70.1% | 69.6% |
| Reconstructed $m_W$ and $m_t$ | 66.7% | 66.5% |

Table 5.2: Event selection efficiencies after each preselection criteria for full-hadronic process.

After selecting two b-jets, one needs to select two combinations of quark jets to form two hadronic Ws. The combination is determined by minimizing the $\chi^2$. Nevertheless the reconstructed information still suffers from the combinatorial backgrounds compared to semi-leptonic process. Reconstructed mass distribution of W and top are shown in the Fig. 5.10

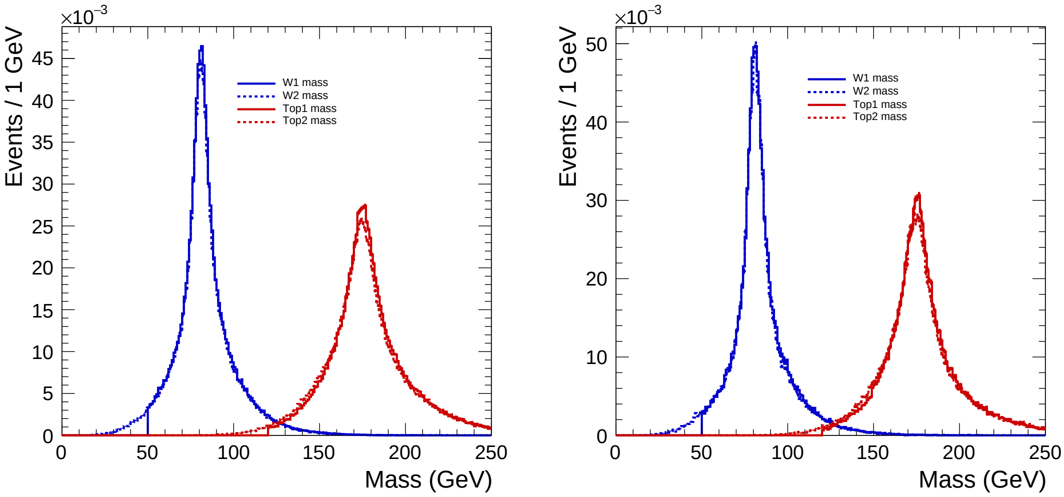

FIGURE 5.10: Reconstructed invariant mass distributions of $e^-_L e^+_R$ (left) and $e^-_R e^+_L$ (right) in full-hadronic channel.

## 5.9 Charge Combination

When the top charge is wrongly reconstructed to be opposite charge, its polar angle will be identified as 180° opposite to the original angle. This is called *migration* and it will affect the $A_{FB}$ calculation as we define the forward and backward events based on this quantity. In order to suppress migrations, one can use various charge combinations, which are the methods to compare charge values.

1 VTX × VTX

Compares vertex charge from two b-jets.

2 Kaon × Kaon

Compares kaon charges decayed from two b-jets.

3 VTX × Kaon

Compares vertex charge from one b-jet with kaon charge from another b-jet.

4 VTX × Kaon'
Compares vertex charge from one b-jet with kaon charge from same b-jet.

5 VTX × Lepton
Compares vertex charge from one b-jet with isolated lepton from leptonically decayed $W^{\pm}$.

6 Kaon × Lepton
Compares kaon charge from one b-jet with isolated lepton from leptonically decayed $W^{\pm}$.

7 Lepton
Uses the isolated lepton from leptonically decayed $W^{\pm}$ after cuts on the reconstructed top quality.

Method 1 - 4 only uses the hadronic information ($b$ and $K^{\pm}$ charge), thus can be applied during the full-hadronic analysis. Table 5.4 shows the probability of being used, and purity of charge identification for each methods. Frequently used methods with low charge purity such as method 5 would be considered as source of migrations.

| Methods | Usage | Charge Purity |
|---|---|---|
| VTX × VTX | 22.7% | 92.9% |
| Kaon × Kaon | 8.85% | 89.8% |
| VTX × Kaon | 25.2% | 91.1% |
| VTX × Kaon' | 19.8% | 92.4% |
| VTX × Lepton | 72.3% | 63.9% |
| Kaon × Lepton | 45.1% | 58.2% |
| Lepton | 72.2% | 95.4% |

TABLE 5.3: Probability of method usage and their purity for semi-leptonic process.

| Methods | Usage | Charge Purity |
|---|---|---|
| VTX × VTX | 45.4% | 90.9% |
| Kaon × Kaon | 16.5% | 87.5% |
| VTX × Kaon | 56.3% | 88.3% |
| VTX × Kaon’ | 46.4% | 89.6% |

Table 5.4: Probability of method usage and their purity for full-hadronic process.

# Chapter 6

# Background

## 6.1 Combinatorial Background

Upon reconstructing top quarks, one has to identify the correct combination of b quark and W boson. As it was discussed in section 5.7, cut on $\chi^2_{top}$ is used to effectively reject wrong combinations. This is combinatorial background and efficiency of reconstructing the correct combination is discussed in this section.

## 6.2 Standard Model Background

The main background processes are listed in the table 6.1. Major Standard Model background processes can be rejected through kinematical cuts for $t\bar{t}$. ILD facilitates the well separation between $b$ and $c$ jets thus the background from the fermion pair production. Different kinematic cuts have been applied for semi-leptonic and full-hadronic channels as one does not contain isolated lepton.

## 6.3 Single Top

The Feynman diagram for the single top production through $e^+e^- \to W^-t\bar{b} \to W^+W^-b\bar{b}$ is depicted in the Fig. 6.1. There are two ways which can produce single top events: t-channel, which contains electron neutrino as a mediator and s-channel which W pair from the $Z^0/\gamma$. Both process leave W and $b$ pair as a final

| Process | $\sigma_{unpol.}$ (fb) | $\sigma_{e^-_L e^+_R}$ (fb) | $\sigma_{e^-_R e^+_L}$ (fb) |
|---|---|---|---|
| $t\bar{t}$ | 572 | 1564 | 724 |
| $u\bar{u} + d\bar{d} + c\bar{c} + s\bar{s}$ | 2208 | 6032 | 2793 |
| $b\bar{b}$ | 372 | 1212 | 276 |
| $\gamma Z^0$ | 11185 | 25500 | 19126 |
| $WW$ | 6603 | 26000 | 150 |
| $Z^0Z^0$ | 422 | 1106 | 582 |
| $Z^0WW$ | 40 | 151 | 8.7 |
| $Z^0Z^0Z^0$ | 1.1 | 3.2 | 1.22 |

Table 6.1: List of Standard Model background channels and each cross sections of different polarizations. [2]

state and this is identical to the top pair production events.

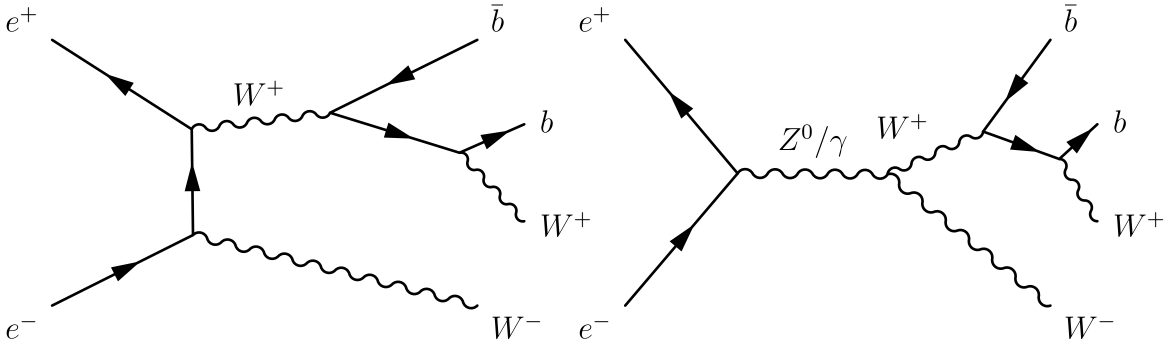

Figure 6.1: t-channel (left) and s-channel (right) of Feynman diagram for single top production

The single top production at $\sqrt{s} = 500$ GeV is 3.1 fb. Therefore, rejection of such event upon analysis of top pair production become substantial both in generated and reconstructed information. Although there is no robust algorithm to separate these process, one can isolate single top event by setting selection criteria to the parton level top mass.

In the parton level, WHIZARD generates events with final states of the type $\ell\nu q_1 q_2 b_1 b_2$ for semi-leptonic and $q_1 q_2 q_3 q_4 b_1 b_2$ for full-hadronic channel, which are mostly from top pair production. Since WHIZARD does not defines the entire intermediate states, one needs to combine the W and $b$ quark mass to know the MC top quark mass. In order to isolate single top events, we used following criterion:

$$|m_{Wb} - m_t^{MC}| > 15 \text{ GeV} \tag{6.1}$$

which was also used in Reference [24]. Generated top mass distribution before and after single top rejection is shown in the Fig. 6.2. From this criterion, 12% of the generated events are from the single top process for $e_R^+e_L^-$ and 6% for $e_L^+e_R^-$ events.

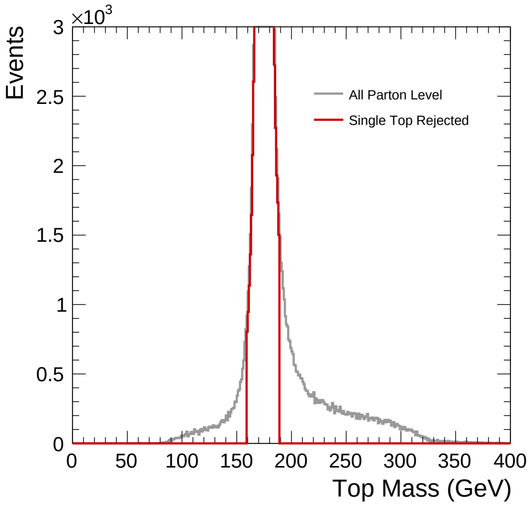

FIGURE 6.2: MC top mass distribution.

The number of single top events compared to top pair production is very small, which is expected since the W$b$ pair mass and the beam energy should be already rejected by the $\chi^2$ cut. Nevertheless, its effect is visible when $A_{FB}$ value is calculated. Fig. 6.3 shows the polar angle distribution and $A_{FB}$ values before and after the single top rejection.

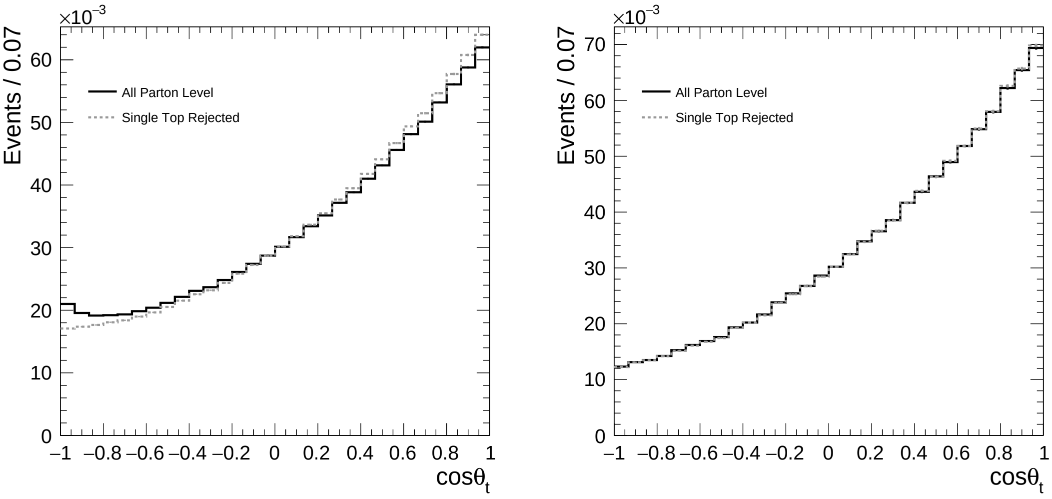

Figure 6.3: Polar angle distribution of top quark before and after the single top removal. Left plot shows the $e^-_L e^+_R$ and right plot shows the $e^-_L e^+_R$ sample.

# Chapter 7

# Results

## 7.1 Semi-Leptonic Channel

As discussed in section 4.1, semi-leptonic channel of the top quark pair, $t\bar{t} \to b\bar{b}q\bar{q}'\ell\nu$, leaves a single isolated lepton and four jets as final state. Therefore, one can use isolated lepton charge as a charge identifier for this process. The polar angle of the top quark is calculated from the decay products of the hadronically decaying top. For this the following considerations apply:

- Regardless of the polarization, there's a chance for the mis-combination of b-jet and W to reconstruct a top quark.
- In the $e^-_R e^+_L$ case, due to the V-A structure, W boson become hard and b jet become soft. W jet will be emitted along the top flight direction, while b-jet will be emitted on the opposite direction. Thus, the reconstruction of top quark momentum is dominated by energetic W jets. Consequently, it will be less vulnerable to the association of wrong b-jets to the W jets.
- In the $e^-_L e^+_R$ case, the b jets become hard and W boson become soft. b-jet will be emitted along the top flight direction, while W jet will be emitted on the opposite direction. Thus, the reconstruction of top quark momentum is dominated by energetic b-jets. Consequently, it will be less vulnerable to the association of wrong W jets to the b-jets.

$W \to \tau\nu$ process was discarded since $\tau$ requires additional clusterization to reconstruct the events.

### 7.1.1 The Forward Backward Asymmetry

Polar angle of fully polarized $e^-_L e^+_R$ case is plotted to demonstrate the reconstruction of top quark. (Fig. 7.1 left) Cuts listed in table 5.1 and all of the methods described in the section 5.9 are applied. Single top rejection is applied at generator level. In both plots, the generator distribution with (green line) and without (blue line) single top rejection was overlayed. One can see that apart from the region $-0.4 < \cos\theta_t < 1$, which is expected to be contaminated by single-top events, the polar angle is well reconstructed. In order to compare semi-leptonic analysis result with full-hadronic analysis, polar angle distribution only using method 1 (VTX × VTX) is plotted in fig. 7.2.

The polar angle of fully polarized $e^-_R e^+_L$ case is shown in the fig. 7.1 right. As explained above, the distribution is less vulnerable to migration due to a wrong association of $b$ and W jets. Therefore all events available after the $t\bar{t}$ selection given in Table 6.1 do enter this distribution.

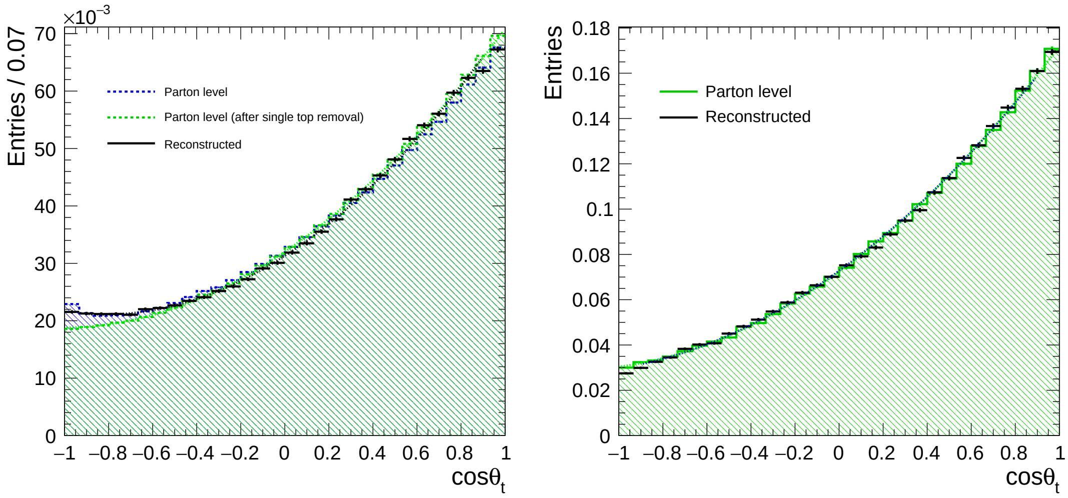

FIGURE 7.1: Top polar angle of fully polarized $e^-_L e^+_R$ (left) and $e^-_R e^+_L$ (right) in semi-leptonic channel.

In order to give the realistic running scenario, mixing of the left and right-handed polarized beams was considered. Given the large electron beam polarization the resulting spectrum is not much different from that for full beam polarization. Fig. 7.3 shows the polar angle distribution of $t\bar{t}$ of generated and reconstructed samples. Cut described in table 5.2 is applied and all of the methods described in the section 5.9 is applied. Left side of the plot is the top polar angle distribution for $(\mathcal{P}_{e^-}, \mathcal{P}_{e^+}) = (-0.8, +0.3)$ and the right side is the one for $(\mathcal{P}_{e^-}, \mathcal{P}_{e^+}) =$

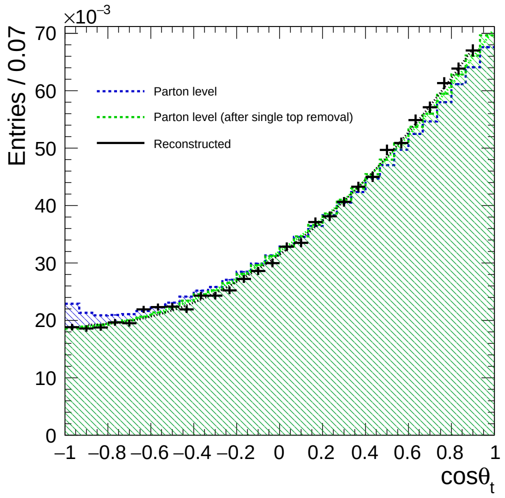

FIGURE 7.2: Top polar angle of fully polarized $e^-_L e^+_R$ only using method 1 as charge identifier.

$(+0.8, -0.3)$. Both in left-handed and right-handed cases, the polar angle spectrum is accurately reconstructed in the region between $-0.4 < \cos\theta_t < 1$. This is due to the accumulation of single top events in the reconstructed events while it was removed for the generator level. This effect is also shown in the Fig. 6.3.

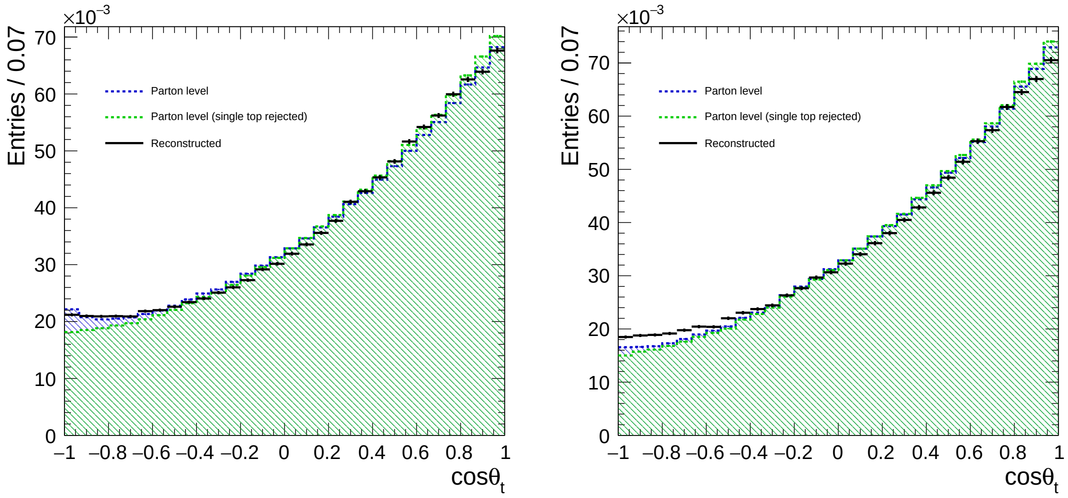

FIGURE 7.3: Top polar angle of $e^-_L e^+_R$ (left) and $e^-_R e^+_L$ (right) in semi-leptonic channel with polarization mixing.

A $b$ quark decayed from a top quark can be an analyzer of the top helicity. One can extract the electroweak couplings also from the $b$ distribution while being protected from wrong combinations. The polar angle spectrum for the b-jets decayed from top quarks are also shown in the Fig. 7.4. For the left-handed case, reconstruction of b-jet polar angle is accurately done between $-0.9 < \cos\theta_b < 0.9$. Near the endcap region, reconstruction fails due to the acceptance of the detector. Same effect is also visible for the right-handed case, while not as accurate as left-handed case.

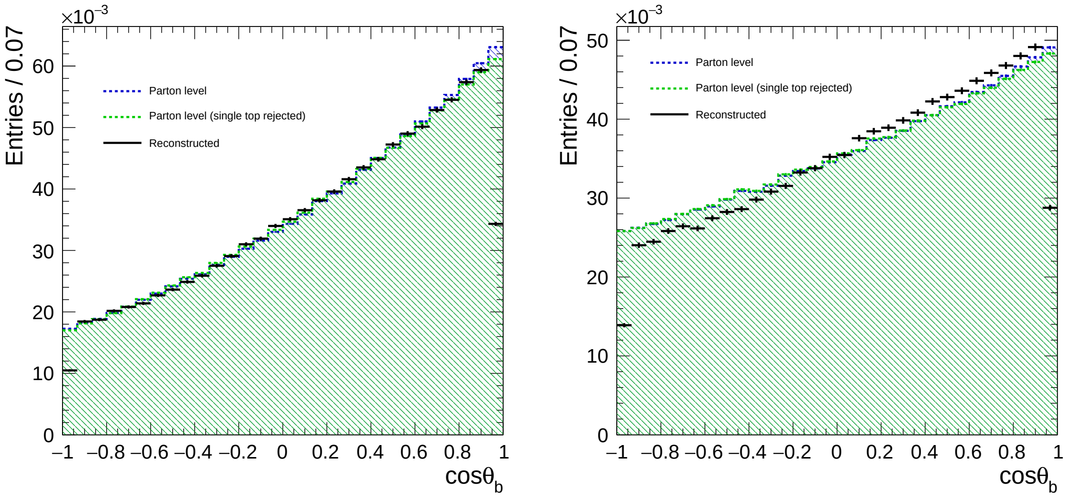

FIGURE 7.4: B polar angle of $e^-_L e^+_R$ (left) and $e^-_R e^+_L$ (right) in semi-leptonic channel.

The forward backward asymmetry $A^t_{FB}$, is defined as:

$$A^t_{FB} = \frac{N(\cos\theta_t > 0) - N(\cos\theta_t < 0)}{N(\cos\theta_t > 0) + N(\cos\theta_t < 0)} \tag{7.1}$$

where $\theta_t$ is the polar angle of top quark. We define the direction along the electron beam line to be "forward" and the opposite of this to be "backward". In case of anti-top, $\theta_t$ is inverted with $\pi$. $A^t_{FB}$ was calculated, using the realistic beam polarization of $(\mathcal{P}_{e^-}, \mathcal{P}_{e^+}) = (\mp 0.8, \pm 0.3)$. The statistical uncertainty of $A^t_{FB}$ was evaluated by:

$$\delta_{A^t_{FB}} = \sqrt{\left(\frac{\partial A^t_{FB}}{\partial N_F}\Delta N_F\right)^2 + \left(\frac{\partial A^t_{FB}}{\partial N_B}\Delta N_B\right)^2} \tag{7.2}$$

where $N_F$ and $N_B$ are the number of reconstructed top events towards forward and backward direction, respectively. Table 7.1 lists the result of $A^t_{FB}$ calculation.

## 7.2 Full Hadronic Channel

Full-hadronic channel of the top quark pair, $t\bar{t} \to b\bar{b}q\bar{q}'q\bar{q}'$, yields six jets as a final state. Full-hadronic channel is vulnerable to the combinatorial background. On

| $(\mathcal{P}_{e^-}, \mathcal{P}_{e^+})$ | $(-0.8, +0.3)$ | $(+0.8, -0.3)$ |
|---|---|---|
| $A^t_{FB,gen}$ | 0.364 | 0.409 |
| $A^t_{FB,reco}$ | 0.345 | 0.369 |
| $\delta_{A^t_{FB}}$ | $2.48 \times 10^{-3}$ | $1.96 \times 10^{-3}$ |
| Efficiency | 34.6% | 32.5% |

Table 7.1: Result of $A^t_{FB}$ calculation from the generated and reconstructed samples with integrated luminosity of 2200 fb$^{-1}$ for each beams.

top of b jet reconstruction, W jets must be reconstructed from four quark jets. This is done by $\chi^2$ minimization method as mentioned in the section 5.7. W mass is used for the minimization yet other parameters is subject to further studies. In addition, the b-jet momentum is required to be $p_b > 30$ GeV which is tighter compared to semi-leptonic analysis.

### 7.2.1 The Forward Backward Asymmetry

Fig. 7.5 shows the polar angle distribution of $e^-_L e^+_R$ and $e^-_R e^+_L$ process. Left plot shows the top polar angle distribution for $(\mathcal{P}_{e^-}, \mathcal{P}_{e^+}) = (-0.8, +0.3)$ and the right plot for $(\mathcal{P}_{e^-}, \mathcal{P}_{e^+}) = (+0.8, -0.3)$.

As mentioned in 7.1, reconstructed top quark momentum is dominated by the $b$ momentum in the case of left-handed electron beam case. Thus the polar angle is well reconstructed in this case.

On the other hand, the reconstruction is more involved for the right handed polarization in full-hadronic channel. In the right-handed case, b-jet is no longer emitted to the same direction as top quark with aforementioned reason and W-jet will fly in the same direction as top. In fact two sets of Ws must be reconstructed out from four quark jets. Hence, there is a greater chance of miscombining the jets to reconstruct both W and top quarks. The top polar angle distribution of $(\mathcal{P}_{e^-}, \mathcal{P}_{e^+}) = (+0.8, -0.3)$ demonstrates this.

The definition of $A^t_{FB}$ is given by Eq. 7.1. Similarly to the semi-leptonic process, $A^t_{FB}$ and its uncertainty $\delta_{A^t_{FB}}$ were evaluated and these values are shown in the table 7.2.

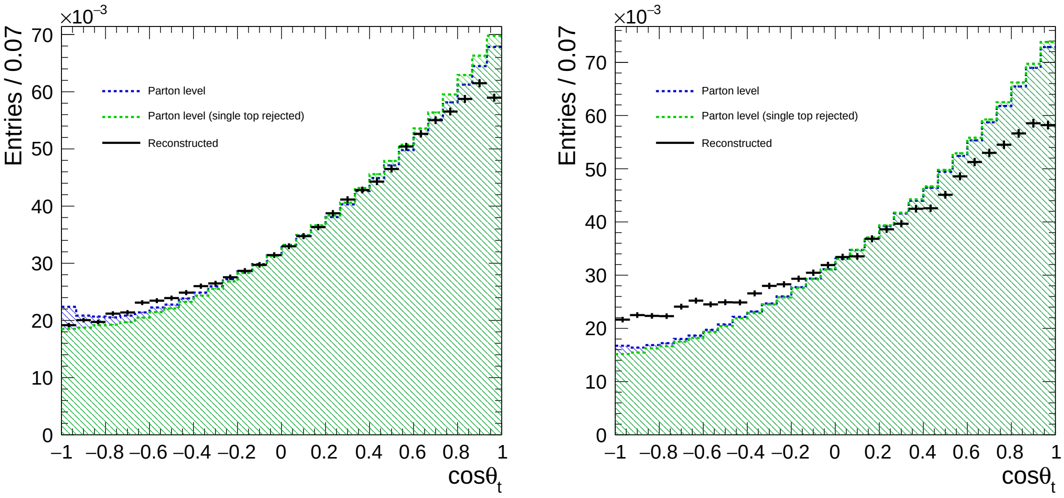

FIGURE 7.5: Top polar angle of $e^-_L e^+_R$ (left) and $e^-_R e^+_L$ (right) in full-hadronic channel.

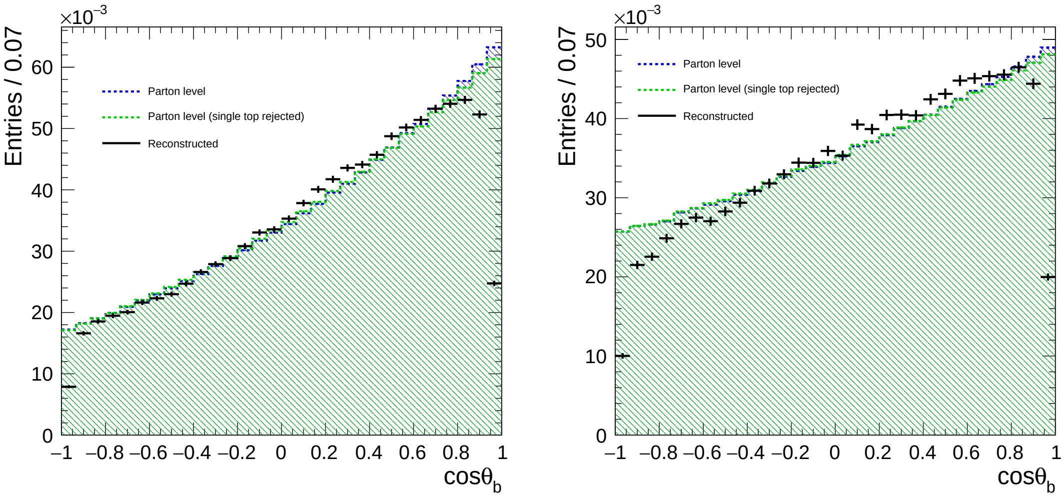

FIGURE 7.6: B polar angle of $e^-_L e^+_R$ (left) and $e^-_R e^+_L$ (right) in full-hadronic channel.

| $(\mathcal{P}_{e^-}, \mathcal{P}_{e^+})$ | $(-0.8, +0.3)$ | $(+0.8, -0.3)$ |
|---|---|---|
| $A^t_{FB,gen}$ | 0.359 | 0.409 |
| $A^t_{FB,reco}$ | 0.322 | 0.284 |
| $\delta_{A^t_{FB}}$ | $2.76 \times 10^{-3}$ | $4.85 \times 10^{-3}$ |
| Efficiency | 11.2% | 9.58% |

TABLE 7.2: Result of $A^t_{FB}$ calculation from the generated and reconstructed samples.

# Chapter 8

# Summary and Discussion

## 8.1 Summary

The heavy quarks have masses comparable to the electroweak vacuum expectation value. The top quark is heaviest elementary particle known today. Therefore, the precise measurements on the heavy quark properties is essential for the indirect searches of the new particle beyond the Standard Model predictions to differentiate them from the various other theories.

In this study, $e^+e^- \to t\bar{t}$ process with polarized beams at $\sqrt{s} = 500$ GeV was analyzed using the full simulation of the ILD detector and both, semi-leptonic ($t\bar{t} \to b\bar{b}W^+W^- \to b\bar{b}q\bar{q}\ell\nu$) and full-hadronic ($t\bar{t} \to b\bar{b}W^+W^- \to b\bar{b}q\bar{q}q\bar{q}$) channel were investigated.

For the semi-leptonic channel, isolated lepton charge, vertex charge and kaon charge were used to identify the reconstructed top charge and 7 different methods were established for the charge comparison scheme and each combination of charges were evaluated. At the total integrated luminosity of $\mathcal{L} = 2200$ fb$^{-1}$, with electron and positron polarization state of $(\mathcal{P}_{e^-}, \mathcal{P}_{e^+}) = (\pm 0.8, \pm 0.3)$, polar angle distribution of top quark was reconstructed in order to calculate the forward-backward asymmetry parameter $A^t_{FB}$. As a result, $A^t_{FB} = 0.345$ was obtain for $(\mathcal{P}_{e^-}, \mathcal{P}_{e^+}) = (-0.8, +0.3)$ polarization with statistical uncertainty of $\delta_{A^t_{FB}} = 2.48 \times 10^{-3}$ and reconstruction efficiency of 34.6%. For the $(\mathcal{P}_{e^-}, \mathcal{P}_{e^+}) = (+0.8, -0.3)$ polarization, $A^t_{FB} = 0.369$ with statistical uncertainty of $\delta_{A^t_{FB}} = 1.96 \times 10^{-3}$, and reconstruction efficiency of 32.5% was obtained. For the first time, the reconstructed $b$ quark polar angle distribution decayed from top quarks was presented. This revealed the acceptance drop at the high polar angle due to the poor $b$-jet reconstruction. Nonetheless, the reconstruction was accurately done for $|\cos\theta < 0.8|$ region.

For the full-hadronic channel, $t\bar{t}$ were distinguished by only using kaon and vertex charge information. As a result, $A^t_{FB} = 0.322$ was obtained for $(\mathcal{P}_{e^-}, \mathcal{P}_{e^+}) = (-0.8, +0.3)$ polarization with statistical uncertainty of $\delta_{A^t_{FB}} = 2.76 \times 10^{-3}$, while $A^t_{FB} = 0.284$ was obtained for $(\mathcal{P}_{e^-}, \mathcal{P}_{e^+}) = (+0.8, -0.3)$ polarization with statistical uncertainty of $\delta_{A^t_{FB}} = 4.85 \times 10^{-3}$.

## 8.2 Future Prospect

Although the polar angle spectrum for $(\mathcal{P}_{e^-}, \mathcal{P}_{e^+}) = (-0.8, +0.3)$ is well reconstructed in full-hadronic channel, the analysis still suffer from the loss in the efficiency as the final efficiency is dropped down to 11% of the entire events. At the moment a consistent result between all methods to measure the b charge is required. One may increase the statistics by accepting the event already if reliable methods as e.g. the vertex charge give a consistent result.

# Bibliography

[1] J-C Brient, P. Dauncey, Erika Garutti, Imad Laktineh, R. Poeschl, Jose Repond, F. Sefkow, Tohru Takeshita, D. Ward, and J. Yu. Calice report to the calorimeter r&d review panel. *arXiv E-Print (only) (2007),*, 08 2007.

[2] M. S. Amjad et al. A precise characterisation of the top quark electro-weak vertices at the ILC. *Eur. Phys. J.*, C75(10):512, 2015. doi: 10.1140/epjc/s10052-015-3746-5.

[3] C. S. Wu, E. Ambler, R. W. Hayward, D. D. Hoppes, and R. P. Hudson. Experimental test of parity conservation in beta decay. *Phys. Rev.*, 105:1413–1415, Feb 1957. doi: 10.1103/PhysRev.105.1413. URL https://link.aps.org/doi/10.1103/PhysRev.105.1413.

[4] S. L. Glashow. Partial Symmetries of Weak Interactions. *Nucl. Phys.*, 22:579–588, 1961. doi: 10.1016/0029-5582(61)90469-2.

[5] Steven Weinberg. A model of leptons. *Phys. Rev. Lett.*, 19:1264–1266, Nov 1967. doi: 10.1103/PhysRevLett.19.1264. URL https://link.aps.org/doi/10.1103/PhysRevLett.19.1264.

[6] Abdus Salam. Weak and Electromagnetic Interactions. *Conf. Proc.*, C680519:367–377, 1968. doi: 10.1142/9789812795915_0034.

[7] M. Tanabashi et al. Review of particle physics. *Phys. Rev. D*, 98:030001, Aug 2018. doi: 10.1103/PhysRevD.98.030001. URL https://link.aps.org/doi/10.1103/PhysRevD.98.030001.

[8] Ties Behnke, James E. Brau, Brian Foster, Juan Fuster, Mike Harrison, James McEwan Paterson, Michael Peskin, Marcel Stanitzki, Nicholas Walker, and Hitoshi Yamamoto. The International Linear Collider Technical Design Report - Volume 1: Executive Summary. 2013.

[9] M. Kobayashi et al. Cosmic ray tests of a GEM-based TPC prototype operated in Ar-CF4-isobutane gas mixtures. *Nucl. Instrum. Meth.*, A641:37–47, 2011. doi: 10.1016/j.nima.2011.02.042,10.1016/j.nima.2012.09.016. [Erratum: Nucl. Instrum. Meth.A697,122(2013)].

[10] Jérémy Rouëné. *A Highly Granular Silicon-Tungsten Electromagnetic Calorimeter and Top Quark Production at the International Linear Collider*. PhD thesis, Orsay, LAL, 2014. URL https://tel.archives-ouvertes.fr/tel-01062136.

[11] Makoto Kobayashi and Toshihide Maskawa. CP-Violation in the Renormalizable Theory of Weak Interaction. *Progress of Theoretical Physics*, 49 (2):652–657, 02 1973. ISSN 0033-068X. doi: 10.1143/PTP.49.652. URL https://doi.org/10.1143/PTP.49.652.

[12] Nicola Cabibbo. Unitary Symmetry and Leptonic Decays. *Phys. Rev. Lett.*, 10:531–533, 1963. doi: 10.1103/PhysRevLett.10.531. [,648(1963)].

[13] Carl R. Schmidt. Top quark production and decay at next-to-leading order in e+ e- annihilation. *Phys. Rev.*, D54:3250–3265, 1996. doi: 10.1103/PhysRevD.54.3250.

[14] W. Kilian, F. Bach, T. Ohl, and J. Reuter. WHIZARD 2.2 for Linear Colliders. In *International Workshop on Future Linear Colliders (LCWS13) Tokyo, Japan, November 11-15, 2013*, 2014.

[15] Wolfgang Kilian, Thorsten Ohl, and Jurgen Reuter. WHIZARD: Simulating Multi-Particle Processes at LHC and ILC. *Eur. Phys. J.*, C71:1742, 2011. doi: 10.1140/epjc/s10052-011-1742-y.

[16] Torbjorn Sjostrand, Stephen Mrenna, and Peter Z. Skands. PYTHIA 6.4 Physics and Manual. *JHEP*, 05:026, 2006. doi: 10.1088/1126-6708/2006/05/026.

[17] M Frank, F Gaede, C Grefe, and P Mato. DD4hep: A detector description toolkit for high energy physics experiments. *Journal of Physics: Conference Series*, 513(2):022010, jun 2014. doi: 10.1088/1742-6596/513/2/022010. URL https://doi.org/10.1088%2F1742-6596%2F513%2F2%2F022010.

[18] Philip Bambade et al. The International Linear Collider: A Global Project. 2019.

[19] Taikan Suehara and Tomohiko Tanabe. LCFIPlus: A Framework for Jet Analysis in Linear Collider Studies. *Nucl. Instrum. Meth.*, A808:109–116, 2016. doi: 10.1016/j.nima.2015.11.054.

[20] M. Boronat, J. Fuster, I. García, E. Ros, and M. Vos. A robust jet reconstruction algorithm for high-energy lepton colliders. *Physics Letters B*, 750:95 – 99, 2015. ISSN 0370-2693. doi: https://doi.org/10.1016/j.physletb.2015.08.055. URL http://www.sciencedirect.com/science/article/pii/S0370269315006565.

[21] D. Bailey et al. The LCFIVertex package: vertexing, flavour tagging and vertex charge reconstruction with an ILC vertex detector. *Nucl. Instrum. Meth.*, A610:573–589, 2009. doi: 10.1016/j.nima.2009.08.059.

[22] Taikan Suehara, Tomohiko Tanabe, and Satoru Yamashita. Improved jet clustering algorithm with vertex information for multi-bottom final states. *Phys. Procedia*, 37:111–118, 2012. doi: 10.1016/j.phpro.2012.03.706.

[23] Sviatoslav Bilokin. *Hadronic showers in a highly granular silicon-tungsten calorimeter and production of bottom and top quarks at the ILC.* PhD thesis, Laboratoire de l'Accélérateur Linéaire, France, 2017. URL https://tel.archives-ouvertes.fr/tel-01946099.

[24] J. Fuster, I. García, P. Gomis, M. Perelló, Eduardo Ros, and Marcel Vos. Study of single top production at high energy electron positron colliders. *Eur. Phys. J.*, C75:223, 2015. doi: 10.1140/epjc/s10052-015-3453-2.